

# On the Early Time X-ray Spectra of Swift Afterglows I: Evidence for Anomalous Soft X-ray Emission

N. R. Butler<sup>1,2</sup>

## ABSTRACT

We have conducted a thorough and blind search for emission lines in  $> 70$  Swift X-ray afterglows of total exposure  $\sim 10^7$ s. We find that most afterglows are consistent with pure power-laws plus extinction. Significant outliers to the population exist at the 5-10% level and have anomalously soft, possibly thermal spectra. Four bursts are singled out via possible detections of 2-5 lines: GRBs 060218, 060202, 050822, and 050714B. Alternatively, a blackbody model with  $kT \sim 0.1 - 0.5$  keV can describe the soft emission in each afterglow. The most significant soft component detections in the full data set of  $\sim 2000$  spectra correspond to GRB 060218/SN 2006aj, with line significances ranging up to  $\sim 20\sigma$ . A thermal plasma model fit to the data indicates that the flux is primarily due to L-shell transitions of Fe at  $\sim$  solar abundance. We associate ( $> 4\sigma$  significant) line triggers in the 3 other events with K-shell transitions in light metals. We favor a model where the possible line emission in these afterglows arises from the mildly relativistic cocoon of matter surrounding the GRB jet as it penetrates and exits the surface of the progenitor star. The emitting material in each burst is at a similar distance  $\sim 10^{12} - 10^{13}$  cm, a similar density  $\sim 10^{17}$  cm $^{-3}$ , and subject to a similar flux of ionizing radiation. The lines may correlate with the X-ray flaring. For the blackbody interpretation, the soft flux may arise from break out of the GRB shock or plasma cocoon from the progenitor stellar wind, as recently suggested for GRB 060218 (Campana et al. 2006). Due to the low  $z$  of GRB 060218, bursts faint in  $\gamma$ -rays with fluxes dominated by this soft X-ray component could outnumber classical GRBs 100-1.

*Subject headings:* gamma rays: bursts — supernovae: general — X-rays: general

---

<sup>1</sup>Townes Fellow, Space Sciences Laboratory, University of California, Berkeley, CA, 94720-7450, USA

<sup>2</sup>Astronomy Department, University of California, 445 Campbell Hall, Berkeley, CA 94720-3411, USA

## 1. Introduction

One of the key open questions in the study of Gamma-ray bursts (GRBs) is that of the X-ray afterglow lines. Claims of low to moderate significance emission lines have been made based on data from several missions: Fe lines have been detected in afterglow data from *ASCA* (Yoshida et al. 1999), *Beppo-SAX* (Piro et al. 1999; Antonelli et al. 2002), and *Chandra* (Piro et al. 2000); lines from highly ionized light, multiple- $\alpha$  elements like Mg, Si, S, Ar, and Ca have been detected in afterglow data from *XMM* (Reeves et al. 2002; Watson et al. 2003) and *Chandra* (Butler et al. 2003). The detections are challenging to explain because they typically imply large, concentrated masses of metals in the circumburst material (see, e.g., Lazzati, Campana, & Ghisellini 1999) and a very efficient reprocessing of the non-thermal afterglow continuum into line radiation (see, Ballantyne & Ramirez-Ruiz 2001; Lazzati, Ramirez-Ruiz, & Rees 2002).

Rutledge & Sako (2003) and Sako, Harrison, & Rutledge (2005) argue that the claims made to date lack the necessary significance needed to prove that the X-ray lines are real. We address the line significance in the case of GRB 011211 in a recent paper (Butler, et al. 2005a) and find that the differing significance estimates are simply due to different input assumption in the continuum modeling. To prove consistency between the analysis techniques utilized by the Reeves et al. (2002) and Rutledge & Sako (2003), we developed software to autonomously detect one or multiple emission lines. Below, we employ the line search tools to comb the vast *Swift X-ray Telescope* (XRT) data set. With nearly 0.4 years in total exposure for  $\gtrsim 70$  bursts observed typically within 1 hour of the GRB, the mounting XRT sample represents a unique laboratory in which we can test the veracity of historical line claims and probe the physics of new phenomena (e.g., flares, rapid and unusually flat light curves) at early times.

As we discuss below, divided up in time, the majority ( $\sim 90\%$ ) of *Swift* X-ray afterglows are well modeled by simple power-laws in energy, partially absorbed below  $\sim 1$  keV by gas along the line of sight. The typical power-law photon index is  $\Gamma \sim 2$ . However, a small fraction ( $\sim 10\%$ ) of the afterglows in the sample exhibit very different spectra ( $\Gamma \sim 5$  power-laws or prominent residuals near 1 keV), which trigger the line detection robot. These spectra can be fit with a blackbody model in addition to a power-law, or with emission lines in addition to the power-law. One such event—GRB 060218 (Cusumano et al. 2006a)—is clearly associated with a SN 2006aj (Mirabal et al. 2006; Sollerman et al. 2006; Modjaz et al. 2006) and may be the smoking gun tying the anomalous soft X-ray spectra from this and 3 other GRB afterglows to supernovae and possibly directly to the breakout of the GRB shock from the progenitor star.

## 2. Data Reduction and Continuum Fits

Our automated pipeline at Berkeley downloads the XRT data in near real time. The burst right ascension and declination are gleaned from the Gamma-ray Coordinates Network (GCN) notices in order to run the `xrtpipeline` reduction task from the HEASoft 6.0<sup>1</sup> software release. We use version 007 of the response matrices. From there, we bin the data in time, exclude pileup chip regions for each time interval, refine the X-ray position, and produce spectra using custom IDL scripts. For the XRT position counting (PC) mode pileup rejection, we discard regions with count rates in excess of 0.5 cts/s (0.5 - 10 keV) (e.g., Nousek et al. 2006). For the Windowed Timing (WT) mode data the cutoff is 150 cts/s. For each time slice, we determined whether or not this threshold has been surpassed by analyzing counts within a 3.5 pixel (inner radius) to 16 pixel (outer radius) annulus around the source. The inner radius is then expanded or contracted to bring the count rate close to (but not beyond) the pileup threshold. For  $\sim 99\%$  of the data by time (or  $\sim 60\%$  by mass), there is no pileup and the resulting inner radius is zero.

Spectral response files are generated using the `xrtmkarf` task for each time slice, and the time slices are weighted by exposure and summed. The spectra are fit in ISIS<sup>2</sup>. For each spectral bin, we require a S/N of 3.5. We define S/N as the background-subtracted number of counts divided by the square root of the sum of the signal counts and the variance in the background. We define the background region as that where the number of counts in an aperture the size of the source extraction region is within 2-sigma of the median background over the chip in that aperture for one contiguous follow-up observation. In most cases, the background is entirely negligible ( $\lesssim 1\%$  of the source flux).

We fit the integrated spectra for each afterglow and also slice the data in time to search for transient emission features. For the PC mode data, we consider data in the 0.3-10 keV energy range, while we restrict to 0.5-10 keV for the WT mode data, where the low energy response appears to be poorly calibrated (see Section 5.4 for more details). For the period between GRBs 050124 and 060313, we reduce data from 72 PC-mode and 44 WT-mode spectra, and sub-divide the PC and WT mode spectra into 208 and 944 spectra, respectively, each with  $\sim 500$  counts. The time coverage of the time-sliced spectra are plotted in Figure 1.

---

<sup>1</sup><http://heasarc.gsfc.nasa.gov/docs/software/lheasoft/>

<sup>2</sup><http://space.mit.edu/CXC/ISIS/>

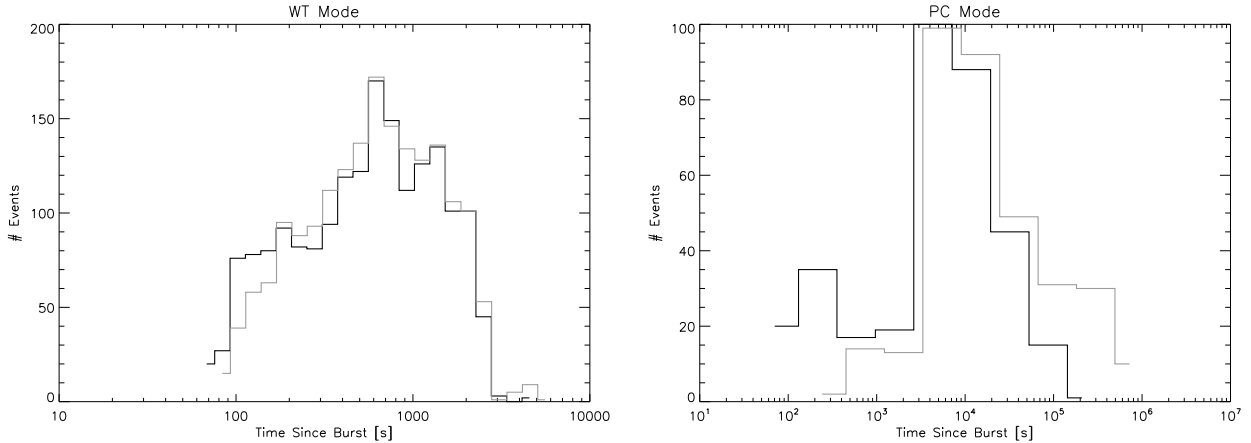


Fig. 1.— (A) Start (black) and stop (grey) times for the WT mode spectra used in our analysis. (B) Start and stop times for the PC mode data. The duration of the WT mode spectra range from 3.5 s to 4.5 ksec, with a median duration of 17s. The PC mode spectra durations range from 113 s to 2.4 Msec, with a median duration of 9.9 ksec.

We test the XRT data against two models for the continuum emission: a power-law and a blackbody model, both with photoelectric absorption. Overwhelmingly, the XRT data are well fit by absorbed power-laws. There is a clear clustering of the photon indices  $\Gamma$ : the median and median absolute deviation about the median are  $\Gamma = 1.9 \pm 0.3$ . (Figure 2B). The median column density in excess of the Galactic value (Dickey & Lockman 1990) is  $N_H - N_{H,\text{Galactic}} = (1.9 \pm 0.9) \times 10^{21} \text{ cm}^{-2}$ , marginally consistent with zero. The integrated (i.e., not time sliced) spectra show consistent values,  $\Gamma = 1.9 \pm 0.2$  and  $N_H - N_{H,\text{Galactic}} = (0.9 \pm 1.2) \times 10^{21} \text{ cm}^{-2}$ . Soft outliers to these trends are labeled in Figure 2 and discussed more below. The fluxes of the spectra cover a broad range (Figure 2C). They are roughly consistent with fluxes previously measured for afterglows by *Beppo-SAX* (Costa et al. 1999).

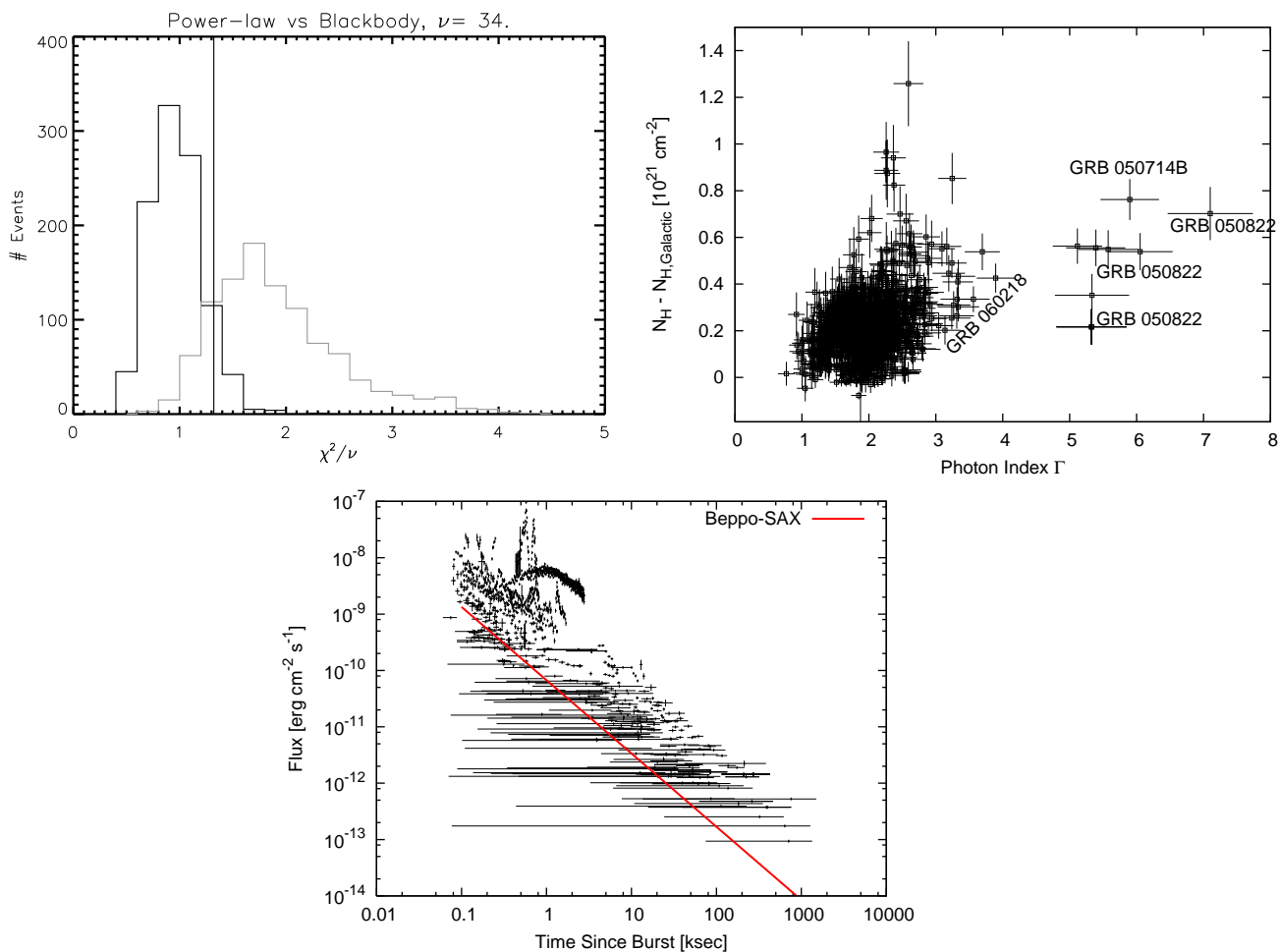


Fig. 2.— (A) Reduced  $\chi^2$  values for the continuum fits, shifted to a fiducial number of degrees of freedom  $\nu = 34$ . The vertical line present the 90% confidence rejection threshold, to the right of which the fit should be rejected. A small fraction of the spectra ( $\sim 10\%$ ) are acceptably fit with a blackbody model (grey line), however most ( $\sim 90\%$ ) are well fit by absorbed power-laws (black line). (B) Continuum parameters  $N_H$  and photon index  $\Gamma$  for the absorbed power-law model fits. There are soft outliers (GRBs 050714B, 050822). (C) Flux vs. time interval plot for the 500 count spectra. Also, plotted is the mean afterglow flux from *Beppo-SAX* (Costa et al. 1999). The *Beppo-SAX* X-ray fluxes are within  $\pm 1$  dex of the red line.

### 3. The Emission Line Search: Efficiency and False Detection Rate

To search for lines in each spectrum, we fit unresolved emission lines in addition to the power-law continuum in the 0.3-5.0 keV band. We allow for the possibility of multiple emission lines (see, e.g., Reeves et al. 2002). The lines are fitted successively, starting with one

line and adding a total of five lines. The best-fit line location at each step is found by convolving the fit residuals with the Line Response Function (LRF) (see, e.g., Rutledge & Sako 2003). The convolution tests for line energies on the  $\delta E = 5$  eV Ancillary Response File grid. The algorithm is described in more detail in Butler, et al. (2005a). We model the LRF versus PI energy bin as a Gaussian with an energy dependent width,  $\sigma(E) = 29.4(E/[1\text{keV}])^{0.355}$  eV. This functional form provides an excellent fit to the core of the XRT LRF. We estimate the significance of each line set by applying the Likelihood Ratio Test (LRT) (also referred to as the  $\Delta\chi^2$  test) to the difference in observed  $\chi^2$  values prior to and after adding the emission line component. These significance estimates are then checked by comparing to the distribution of  $\Delta\chi^2$  produced by a Monte Carlo (MC) simulation (Section 3). We quote significance values in units of normal distribution  $\sigma$ 's (i.e., a null hypothesis probability of  $2.7 \times 10^{-3}$  is  $3\sigma$ ,  $5.7 \times 10^{-7}$  is  $5\sigma$ , etc.).

For a spectrum containing  $\sim 500$  counts, the typical energy binning oversamples the LRF full-width at half max by a factor  $\sim 2$ . By fixing the number of counts in each spectra, it is a simple task to determine MC line significances for the sample as a whole. Such a determination for each spectrum would be prohibitively time consuming. To be sure that we are not missing features due to the 500 count constraint, we have also dyadically grouped (2,4,8, spectra together, etc., up to the full integration) and searched the spectra for each burst. We impose a tighter trigger criteria (see Section 4.4) on these data. In section 5.1, we discuss a line search for the integrated spectra of bright ( $> 10$  cts/s) XRT flares.

Figure 3 displays our triggers for 1-5 emission lines from the blind search through the full data set. Searching 1152 spectra, the trials probability for finding one spectrum with a  $4.5\sigma$  trigger is 99% confidence. Given the sample median, lower and upper quartile values for the observed single-trial trigger significances found —  $1.39\sigma$ ,  $0.94\sigma$ , and  $1.83\sigma$ , respectively,  $4.5\sigma$  is also 3 interquartile lengths from the upper quartile, which is a common measure for strong outliers (e.g., Devore 1995). We find a handful of triggers near or beyond this value, which occur in the spectra of 3 bursts (e.g., Figure 3). As mentioned above, the significance estimates used here come from the LRT test. We also check the validity of this procedure by simulating  $10^5$  spectra with 500 counts each and searching for lines in the simulated spectra. For the simulation, we take  $\Gamma = 2$  and  $N_H = 10^{21} \text{ cm}^{-2}$  as representative values for the entire XRT sample. The resulting (false) trigger rate for the most significant subset of 1-5 emission lines from the search is plotted in blue in Figure 3. There is a clear departure at low significance from the model (dashed curve) for the LRT. Importantly, the departure is negligible and conservative for significances  $\gtrsim 3\sigma$ . The validity and limitations of the LRT are discussed in detail elsewhere (Yaqoob 1998; Protassov et al. 2002).

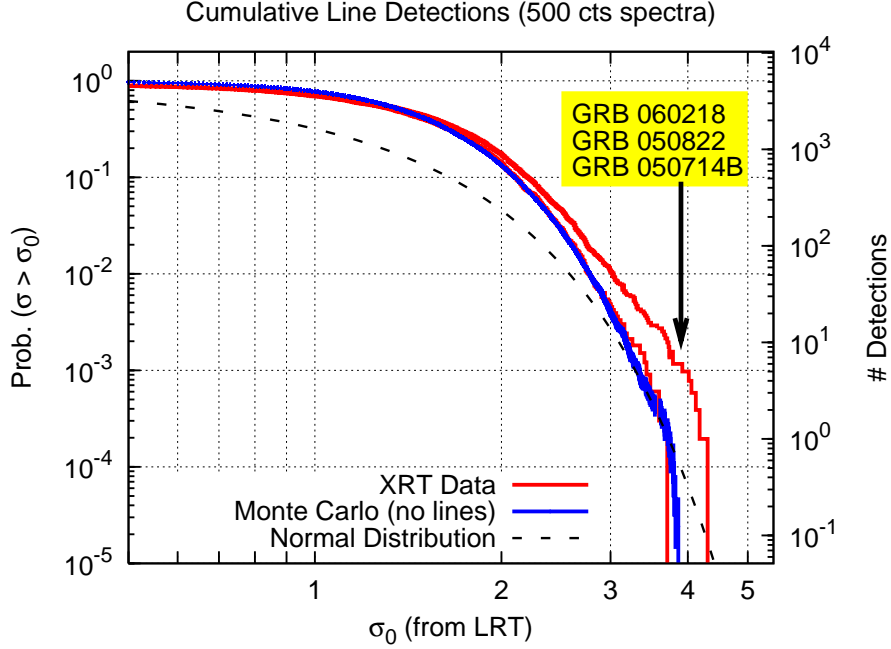


Fig. 3.— The number of triggers (red lines) for 1-5 emission lines in XRT spectra containing  $\sim 500$  counts versus their estimated significance. A branch in the XRT curve is seen depending on whether or not 050714B, 050822, and 060218 are included in the sample. The bottom red curve does not include these events and is roughly consistent (KS-test significance  $\sim 3\sigma$ ) with the Monte Carlo false event rate (blue line). Ignoring the data from the anomalously bright GRB 060218—which comprise  $\sim 30\%$  of the spectra under study—the excluded 2 bursts correspond to 4% of the the full sample spectra. The Monte Carlo curve is determined from  $10^5$  simulations of a fiducial 500 count spectrum (Section 3). The dotted black line is the expected false event for the LRT (i.e., the cumulative normal distribution).

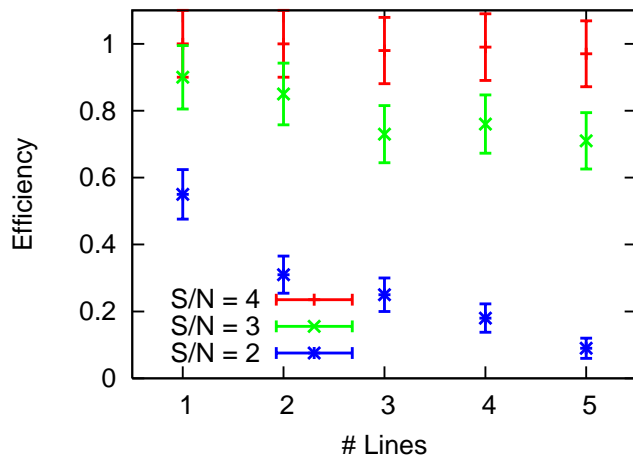


Fig. 4.— The fraction (= efficiency) of  $10^3$  simulated spectra with lines of varying signal to noise ( $S/N$ ) where the trigger algorithm found the lines at their true locations and with consistent  $S/N$  values. The efficiency is near unity for 1-5 emission lines, each with  $S/N \gtrsim 3$ . The efficiency drops sharply for multiple lines with  $S/N \lesssim 2$ .

We also perform simulations to determine the efficiency of the algorithm for detecting lines known to be present. Starting with the same continuum model used for the false trigger tests, we add lines with  $S/N = 3$  (comparable to low  $S/N$  values from lines detected previously) randomly placed in energy over the 0.3-5.0 keV band. Figure 4 displays the efficiency (fraction of iterations where the lines are detected at their true locations) of the algorithm as the assumed line  $S/N$  is varied in the MC. The efficiency drops sharply for  $S/N \lesssim 2$  but remains near unity for  $S/N \gtrsim 3$ . We note that the trigger software autonomously finds (see, Butler, et al. 2005a) each of the 5 emission lines claimed for GRBs 011211 (Reeves et al. 2002) and 030227 (Watson et al. 2003). There is no clear dependence of the efficiency on the line energy, however, the restricted energy band places clear limits on the chemical species to which the search is sensitive. For nearby events ( $z \lesssim 0.4$ ), the upper energy cutoff of 5.0 keV results in non-detection of the Fe- group elements. The low-energy cutoff can inhibit detection of light element lines (e.g., Ne at  $z \gtrsim 2$ , Si at  $z \gtrsim 5$ ). From the simulations, we estimate that LRT significances in  $\sigma$  units are accurate to  $\sim 20\%$  for  $S/N \gtrsim 3$  lines with  $\sigma_{\text{LRT}} \gtrsim 3$ . Potential unresolved emission lines from astrophysically abundant species are detected with high efficiency over a broad range of redshifts. In principle, the search is also sensitive to broad emission lines, which can be built up from the superposition of multiple narrow lines. We now discuss the individual triggers in reverse chronological order.



## 4. Line Emission Detections in Soft Portions of Three X-ray Afterglows

### 4.1. GRB 060218

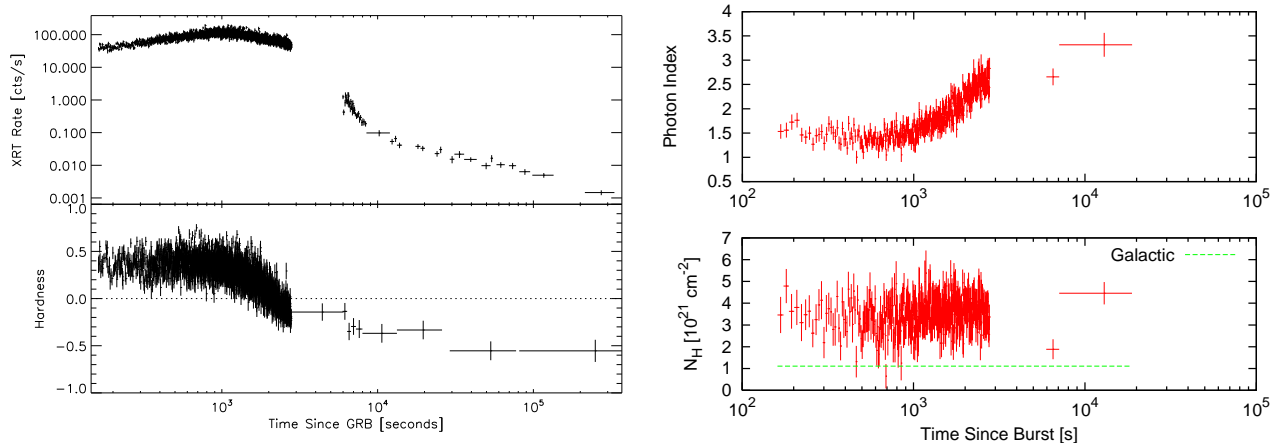


Fig. 5.— (A) The X-ray light curve for the GRB 060218 afterglow. “Hardness” is the difference over the sum of the 1.5–8.0 keV counts and the 0.5–1.5 keV counts. (B) Power-law fits to the afterglow.

The flux from this event was extraordinarily high. The light curve displays a prominent hard to soft evolution during a broad temporal rise, followed by a rapid decline and leveling off (Figure 5). The soft portion of the afterglow (after  $t \sim 1$  msec) accounts for much of the tail of the  $\Gamma \sim 2 - 3$  distribution in Figure 2. A preliminary spectral analysis is reported in Cusumano et al. (2006b). We group the WT (PC) mode counts into 355 (2) spectra, each containing  $\sim 500$  cts. Due to the large data mass, we present our fit results in plot form (Figure 5B) for these finely resolved data, providing tables below for the spectra with  $\sim 16,000$  cts.

Overall, the finely time-sliced data are well fit ( $\chi^2/\nu = 12149.5/12291$  for 356 spectra) with absorbed power-law’s, with  $N_H = (3.8 \pm 0.4) \times 10^{21} \text{ cm}^{-2}$  on average (consistently larger than the Galactic value  $N_{H,\text{Galactic}} = 1.11 \times 10^{21} \text{ cm}^{-2}$ ; Dickey & Lockman 1990). Toward the end of the WT mode data at ( $t = 2.317 - 2.326$  msec), the power-law fit becomes poor ( $\chi^2/\nu = 52.59/32$ , with  $\Gamma = 2.3 \pm 0.2$ ,  $N_H = (3.9 \pm 0.6) \times 10^{21} \text{ cm}^{-2}$ , and unabsorbed flux  $f = (3.1 \pm 0.3) \times 10^{-9} \text{ erg cm}^{-2} \text{ s}^{-1}$  [0.5–10 keV]). The fit is improved at  $4\sigma$  significance ( $\Delta\chi^2 = 24.69$ , for 4 additional degrees of freedom) with the addition of 2 emission lines (Figure 7). The best fit line energies are  $0.82 \pm 0.04$  and  $1.01 \pm 0.04$  keV. For redshifts near  $z = 0.033$  (Mirabal et al. 2006), the lines can be identified with K-shell transitions in H and He-like species of Ne or L-shell transitions from Fe-group elements. The equivalent

widths and luminosities are  $205 \pm 42$  and  $145 \pm 30$  eV and  $3.6 \pm 0.2$  and  $(1.9 \pm 0.2) \times 10^{-10}$  erg cm $^{-2}$  s $^{-1}$ , respectively. The blackbody model provides a poorer fit to the data in this ( $\chi^2/\nu = 82.96/32$ ) and the other time regions. A power-law plus blackbody model provides a mediocre fit ( $\chi^2/\nu = 42.94/30$ ).

As we discuss below, the integrated spectrum is also quite well fit by a thermal MEKAL (Mewe, Gronenschild, & van den Oord 1985) plasma model ( $\chi^2/\nu = 26.90/30$ ) with  $kT = 0.44 \pm 0.06$  and normalization (see note in Table 3)  $3.0 \pm 1.3$  for solar abundances. The  $1\text{-}\sigma$  lower limit on the abundance is 0.2 solar, with an undefined upper limit. The line emission is dominated by L-shell Fe, with an Fe to Ne abundance ratio  $1.5^{+22.5}_{-0.7}$ , relative to solar.

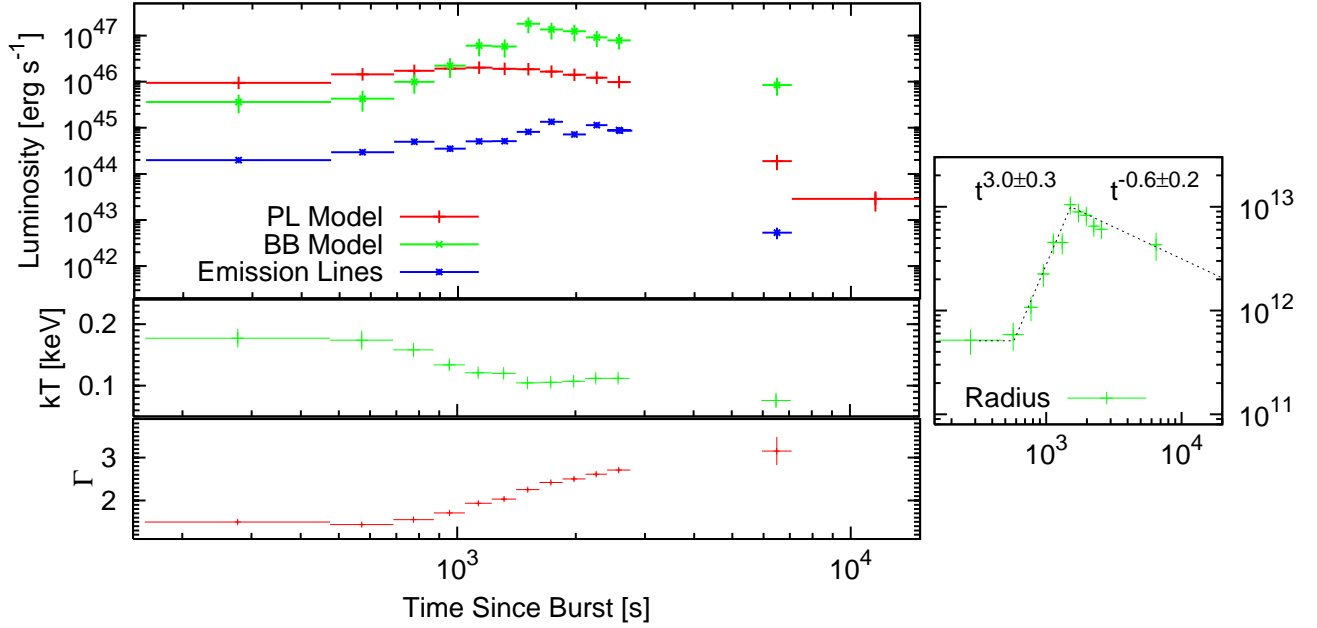


Fig. 6.— A spectral deconvolution for GRB 060218 into soft and hard emission components. The plotted power-law model components (Flux and photon index  $\Gamma$ ) are for the power-law plus blackbody model. The blackbody radius is measured in cm.

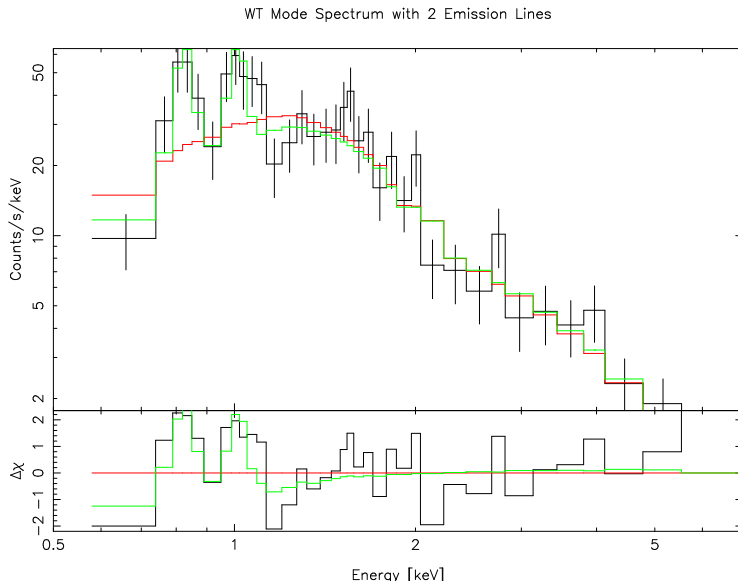


Fig. 7.— The XRT WT Mode spectrum from 2.317 to 2.326 ksec after GRB 060218. Two emission lines at 0.82 and 1.01 keV (green curve), possibly associated with L-shell transitions in Fe at  $z = 0.033$  (Mirabal et al. 2006), improve the power-law fit (red curve) at  $4\sigma$  significance. In the residuals panel, the green curve shows the way the power-law residuals (black curve) are fit by the power-law plus lines model.

There is strong evidence that the soft emission component is present throughout an extended portion of the observation. Only  $\sim 50\%$  of the dyadically grouped spectra containing  $> 500$  cts are found to be adequately fit by the simple absorbed power-law models. Particularly for the spectra containing 16,000 or more counts, a soft component near 1 keV is strongly required (power-law model alone rejected at  $> 90\%$  confidence in 11 of 12 spectra; Table 1). With the inclusion of the blackbody component or emission lines in addition to the power-law, each fit to the  $\sim 16,000$  cts spectra yields  $\chi^2/\nu \lesssim 1$ .

Figure 6 shows the results of the spectral deconvolution of these data into power-law and soft components. The power-law component displays a smooth hard to soft evolution in time. In the case of the emission line model, the lines in the 0.8-1.0 keV energy range, are detected in multiple time intervals (Table 2), with high ( $> 5\sigma$ ) significance triggers coming after  $t \sim 1$  ksec. In addition to the lines at  $E \lesssim 1$  keV discussed above, triggers in the 3-4 keV range are found (Table 2), possibly associated with H- or He-like Ar and Ca.

The soft-component luminosity  $L$  in both cases appears to peak after the power-law component. The blackbody temperature declines mildly after  $t = 580$ s as  $(0.19 \pm 0.01)(t/580\text{s})^{(-0.54 \pm 0.08)}$  keV to  $kT = 0.105 \pm 0.004$  keV at  $t = 1.52$  ksec, then remains constant and possibly declines

at late time. Using the standard formula for the blackbody radius:

$$R_{\text{BB}} = 2.78 \left( \frac{L}{10^{46} \text{erg s}^{-1}} \right)^{1/2} \left( \frac{kT}{0.1 \text{ keV}} \right)^{-2} \times 10^{12} \text{cm}, \quad (1)$$

and  $z = 0.033$  (Mirabal et al. 2006), the blackbody radius increases, peaks, then decreases with the time dependences shown in Figure 6. Here and throughout, we assume a cosmology with  $(h, \Omega_m, \Omega_\Lambda) = (0.65, 0.3, 0.7)$ . We find consistent behavior independent of whether or not we fix  $N_H$  or  $kT$  in the fits. Consistent values for the initial blackbody radius are reported by (Campana et al. 2006). However, they find that the radius continues to grow in time during the XRT observation without peaking, a scenario that we find to be ruled out at the  $\sim 7\sigma$  level.

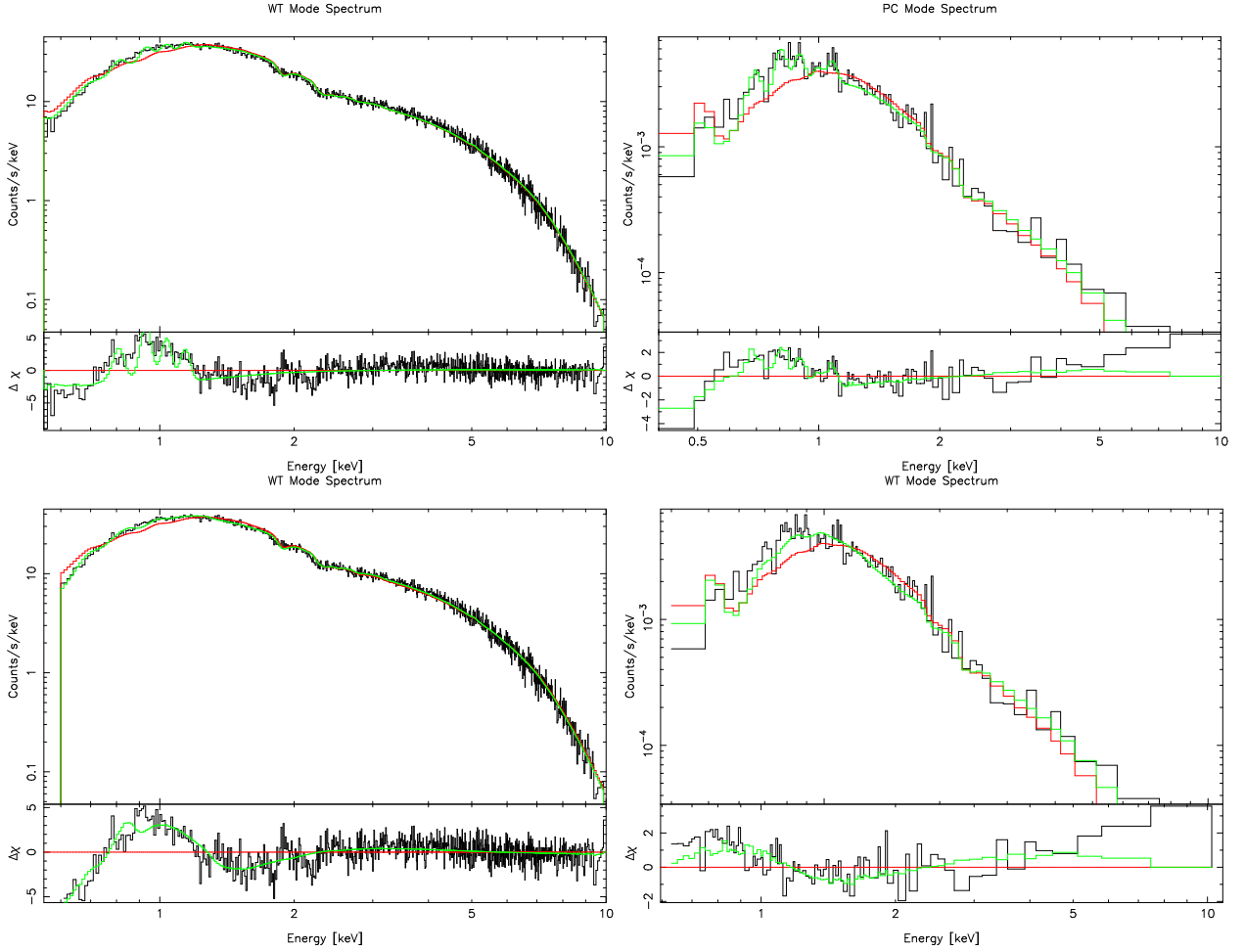


Fig. 8.— Power-law models (red curves) fail to describe the soft emission in the integrated WT mode ( $t = 160\text{s}-2.8\text{ksec}$ ) and PC mode ( $t = 5.9\text{ksec}-3.1\text{Msec}$ ) spectra for GRB 060218 (Table 3). (A) Top two plots. Both data sets are better fit with the addition of 4-5 emission lines (green curves, also plotted for the power-law model residuals): WT mode, 4 lines,  $20.6\sigma$ ,  $\Delta\chi^2 = 460.03$ , for 8 additional degrees of freedom; PC mode, 5 lines,  $6.9\sigma$ ,  $\Delta\chi^2 = 75.37$ , for 10 additional degrees of freedom. (B) Bottom two plots. The fits to both data sets are also markedly improved with the addition of a blackbody continuum component (Table 3).

Figure 8 shows the integrated WT and PC mode spectrum for the afterglow. Continuum spectral fits are reported in Table 3. Prominent residuals are present in both spectra near 1 keV. The WT and PC mode data can be fit with 4 emission lines at energies  $0.80 \pm 0.03$ ,  $0.9 \pm 0.03$ ,  $1.00 \pm 0.03$ , and  $1.1 \pm 0.03$  keV in addition to the power-law continuum. The WT mode trigger is the most significant trigger in the entire sample by a large margin (see Section 4.4). The line luminosities are  $\approx 2 \times 10^{-11}$  erg cm $^{-2}$  s $^{-1}$  in the WT mode spectrum and  $\sim 10^3$  times fainter in the PC mode data. Oppositely, the equivalent widths increase by

a factor  $\sim 5$  from  $\approx 20$  eV in the WT mode data, indicating that the line fluxes decrease less slowly than the continuum flux (see, also, Figure 16). If we relax the upper limit on the line energy search, there is a weak ( $\sim 2\sigma$ ) trigger on a possible K-shell Fe- series line at  $E = 6 \pm 1$  keV in the PC mode spectrum, with an equivalent width of order 1 keV (e.g., residuals in Figure 8B). The further addition of lines to either spectrum does not significantly improve the fits.

The poor apparent  $\chi^2/\nu = 1280.53/760$  in the case of the WT mode data probably should not be taken too seriously, because the flux is high and the inclusion of a small  $\lesssim 5\%$  systematic error component leaves the fit statistically acceptable. The spectra can also be fit with a thermal plasma component (assuming solar abundances) in addition to the power-law (Table 3)—which reinforces the notion that some of the soft emission may be in the form of discrete lines—or with a blackbody in addition to the power-law.

Comparing the hypothesis of emission lines to that of a blackbody (in additional to a non-thermal continuum) for GRB 060218, we find that the event is a particularly strong line candidate. The power-law plus two line model is an excellent fit to the 500 cts spectrum discussed above ( $\chi^2/\nu = 27.9/28$ ), whereas the power-law plus blackbody model fit is mediocre ( $\chi^2/\nu = 42.94/30$ .)

## 4.2. GRB 050822

This event is a clear outlier in Figure 2. A preliminary spectral analysis has been reported by Godet et al. (2005). The spectrum displays a gradual softening in time which increases abruptly with the impulsive flare at  $t \approx 430$ s (Figure 9B). The continuum spectrum during the flare (430s to 550s after the burst) is well-fit by a blackbody (Table 4), with a decreasing temperature in time  $kT = 0.26 - 0.17$  keV (observer frame). There is an indication that the blackbody radius from Equation 1 may increase in time by  $\sim 50\%$ , starting at  $R_{\text{BB}} = (2.7 \pm 0.5) \times 10^{12}$  cm at  $t = 430$ s and peaking at  $R_{\text{BB}} = (4.5 \pm 1.3) \times 10^{12}$  cm at  $t = 490$ s, assuming  $z = 1.2$  (see below).

A power-law model also provides an acceptable fit to the data during the flare, except during the penultimate time interval, 489.5 to 509.4s (interval #14 in Table 4;  $\chi^2/\nu = 54.71/33$ , rejectable at 99% confidence). The blackbody model fit is marginally better in interval #14 ( $\chi^2/\nu = 51.06/33$ , rejectable at 98% confidence) than the power-law fit. An added set of 5 emission lines improves the power-law fit during interval #14 at  $4.4\sigma$  significance ( $\Delta\chi^2 = 40.56$ ,  $\nu = 10$ ; Table 4). The same 5 lines improve the blackbody fit at  $2.8\sigma$  significance ( $\Delta\chi^2 = 25.03$ ,  $\nu = 10$ ). The continuum fit residuals are narrow (Figure 10); neither

the power-law nor the blackbody fit for interval #14 is improved by adding an additional blackbody or power-law continuum component.

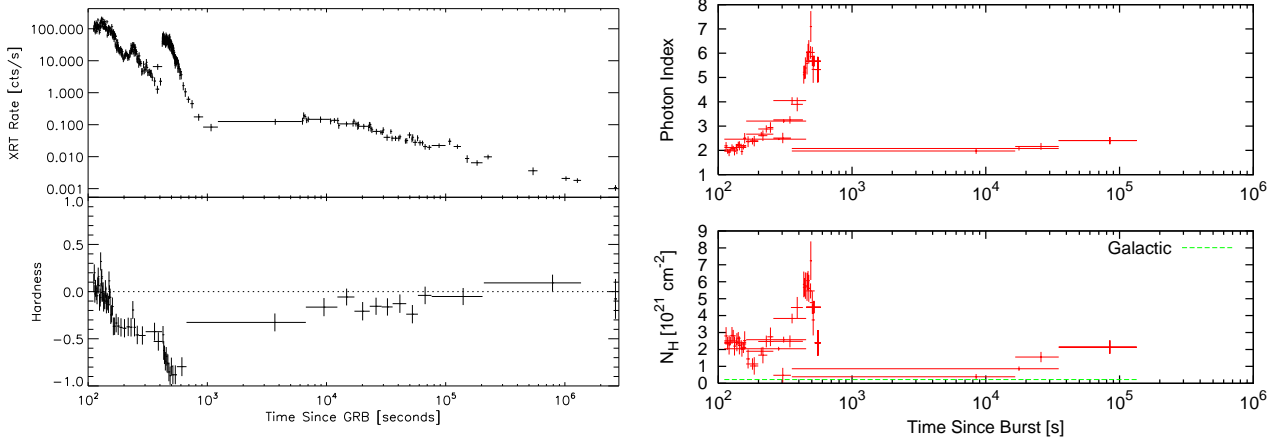


Fig. 9.— (A) The X-ray light curve for the GRB 050822 afterglow. There is a strong flare at  $t \sim 500$ s, during which the spectrum becomes very soft. (B) Spectral evolution for GRB 050822. A dramatic increase in the spectral curvature near 400s is clear from a jump in the photon index and best-fit absorption column.

We test for the presence of the line set found for interval #14 by fitting the best the line set model to the data from the other time intervals. We allow one floating normalization, with the other line parameters fixed relative to this normalization. If the line-set from interval #14 is present during the flare outside of interval #14 (i.e., in intervals 11, 12, 13, and 15), the combined flux from the 5-line set must be lower by a factor  $> 4$  (90% confidence). Thus, the overall or relative flux of each line appears to be changing in time. If we take the  $\sim 20$ s period during which the line triggers are found to be most significant as representative of the period of active line emission, then the possible detection appears very unusual and probably not credible given the models for line emission (Section 5.3 below). We note that there is a weak trigger on the line set at earlier times (intervals #3-#5), with a mean flux consistent with that found for interval #14 but also consistent with zero at the  $1-\sigma$  level.

By hand, we combine the PC and WT mode spectra in the tail of the flare (see Figure 10) and use the PC mode redistribution matrix to perform a fit. The data in this interval (#19 in Tables 4 and 5) are also poorly fit by either continuum model and show modest significance evidence for 5 emission lines. Thus, the very short duration of the line trigger may be due to the detection threshold and may not reflect the physical emission timescale.

The redshift is currently unknown for this event. The line centroids during interval #14 (Table 4) are too closely spaced to allow for an association with H-like ions from light

metals only (e.g., Reeves et al. 2002; Watson et al. 2003). However, if we allow the He-like species, identifications are possible and non-unique. One possible association for the 5 lines in Figure 10B is: Ar XVII, S XVI, S XV, Si XIV, and Si XIII at  $z = 1.2$ . From Table 5, the lines at  $E = 0.81, 0.91, 1.04,$  and  $1.23$  keV are detected in multiple time intervals. A line near 3.5 keV is detected in two time intervals and could be associated with H-like Co or Ni at  $z = 1.2$ . A power-law plus MEKAL model provides a poor fit due to the closely spaced emission lines.

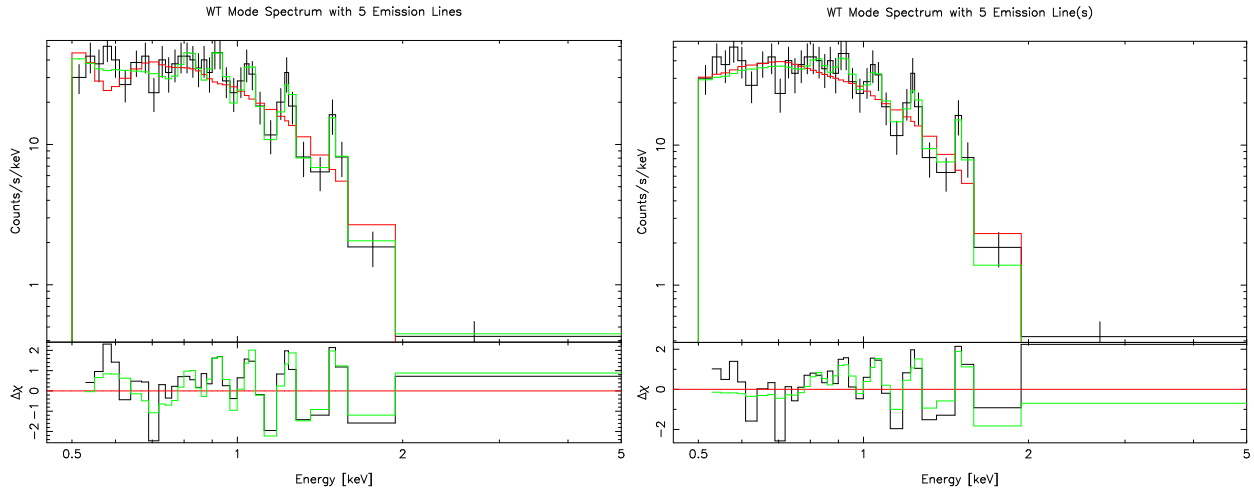


Fig. 10.— (A) In interval #14 during the GRB 050822 flare, emission lines at 0.81, 0.91, 1.04, 1.23, and 1.49 keV (green curve), possibly associated with Si XIII, Si XIV, S XVI, S XV, and Ar XVII at  $z = 1.2$ , improve the power-law model fit (red curve) at  $4.4\sigma$  significance (Table 5). (B) The same but for a blackbody continuum model. The lines are  $2.8\sigma$  significant. For the residuals panel in each plot, the green curves show the way the continuum model residuals (black curves) are fit by the continuum plus lines model.

There is one minor caveat relevant to our analysis of this event. We include two detector columns (RAW X columns #290 and #291) in the WT mode data which are normally discarded in the standard `xrtpipeline` processing. These are neighboring columns (sections of which have been found to behave anomalously) to columns which were damaged as the result of a possible micro-meteorite impact<sup>3</sup>. We find that the continuum spectral fit parameters are consistent whether the columns are retained or rejected. However, because the two columns are near the center of the source extraction region for a large part of the observation, the loss in source flux associated with rejecting the columns mildly reduces the line trigger significance to  $3.5\sigma$ . Here the time extraction is broadened to 480-512s, in order

<sup>3</sup>[http://swift.gsfc.nasa.gov/docs/swift/analysis/xrt\\_digest.html](http://swift.gsfc.nasa.gov/docs/swift/analysis/xrt_digest.html)



to get 510 counts in the spectrum.

Comparing the hypothesis of emission lines to that of a blackbody (in addition to a non-thermal continuum) for GRB 050822, we find that this event, like GRB 060218, is a strong line candidate. The power-law plus five line model provides an excellent fit, ( $\chi^2/\nu = 14.15/23$ ), whereas a power-law plus blackbody improves the power-law fit very little. We note that the line significance degrades (from  $4.4\sigma$  to  $2.8\sigma$ ) if the underlying continuum is assumed to be a blackbody.

### 4.3. GRB 050714B

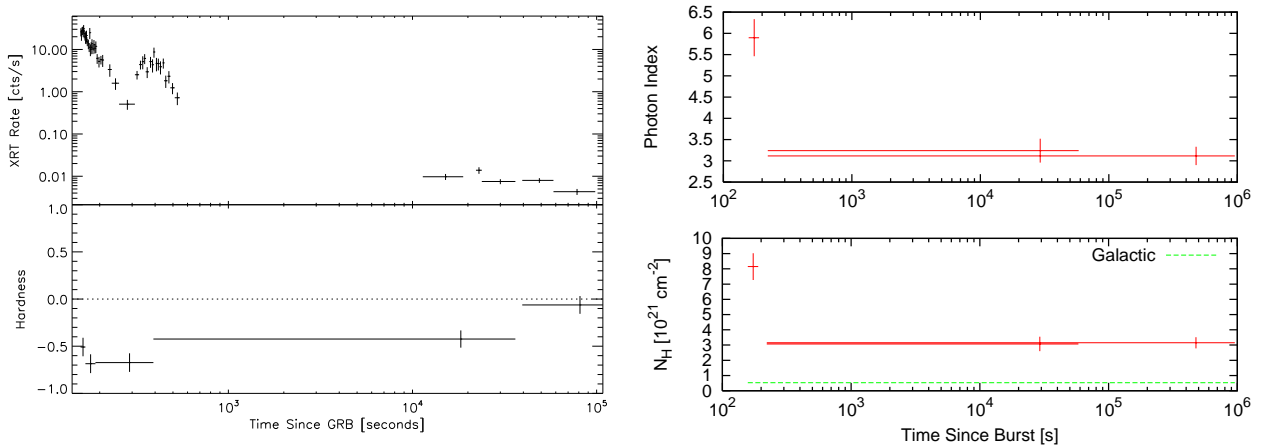


Fig. 11.— (A) The X-ray light curve and hardness plot for GRB 050714B. (B) There is strong spectral evolution during the early X-ray afterglow.

Also a clear outlier in Figure 2, the WT mode spectrum for the time interval 157.4 to 189.7s (#1 in Table 6) corresponds to a rapid decline in the X-ray light curve and is well-fit by a blackbody. Alternatively, the spectrum can be modeled by a power-law with photon index  $\Gamma = 5.9 \pm 0.4$  (see, also, Page et al. 2005a). The spectrum during the flare (PC mode;  $t \approx 275 - 525$ s) is poorly fit by either a blackbody ( $\chi^2/\nu = 97.19/35$ ) or a power-law ( $\chi^2/\nu = 76.78/35$ ). The PC mode spectrum from the start of the flare until 58.3 ksec, can be marginally well fit ( $\chi^2/\nu = 48.64/33$ ) by a power-law plus blackbody. In Table 6, we also extract the PC mode data during the flare only (interval #3) and demonstrate that the same result holds there, although with larger error bars. Between regions #1 and #3, the blackbody temperature in the observer frame decreases from 0.2 to 0.1 keV, and the radius increases from  $R_{\text{BB}} = (2.7 \pm 0.5) \times 10^{12}$  cm to  $(1.2 \pm 0.7) \times 10^{13}$  cm (Equation 1), assuming  $z = 2.66$  (see below).

Alternatively, the power-law fit to interval #2 is improved at  $4.2\sigma$  significance with the inclusion of 4 emission lines ( $\chi^2/\nu = 41.69/27$ ;  $\Delta\chi^2 = 35.09$ ,  $\nu = 8$ ; Figure 12). The fit to region #3 is improved less with the addition of lines, however there is a small number of counts in that hand-selected region, and the line locations are consistent with those from region #2 (Table 7). There are a number of plausible line identifications for region #2. For the lines at  $0.91 \pm 0.03$ ,  $0.76 \pm 0.05$ ,  $0.56 \pm 0.05$ , and  $1.12 \pm 0.05$  keV, one association is made with H-like species Ar XVIII, S XVI, Si XIV, Ca XX, respectively, at  $z = 2.66$ . A thermal (MEKAL) plasma with normalization (see, Table 3)  $0.1 \pm 0.05$  for solar abundances and  $kT = 1.0 \pm 0.2$  keV at a similar redshift ( $z = 2.4$ ), in addition to the power-law, provides an acceptable fit to the data ( $\chi^2/\nu = 44.48/33$ ).

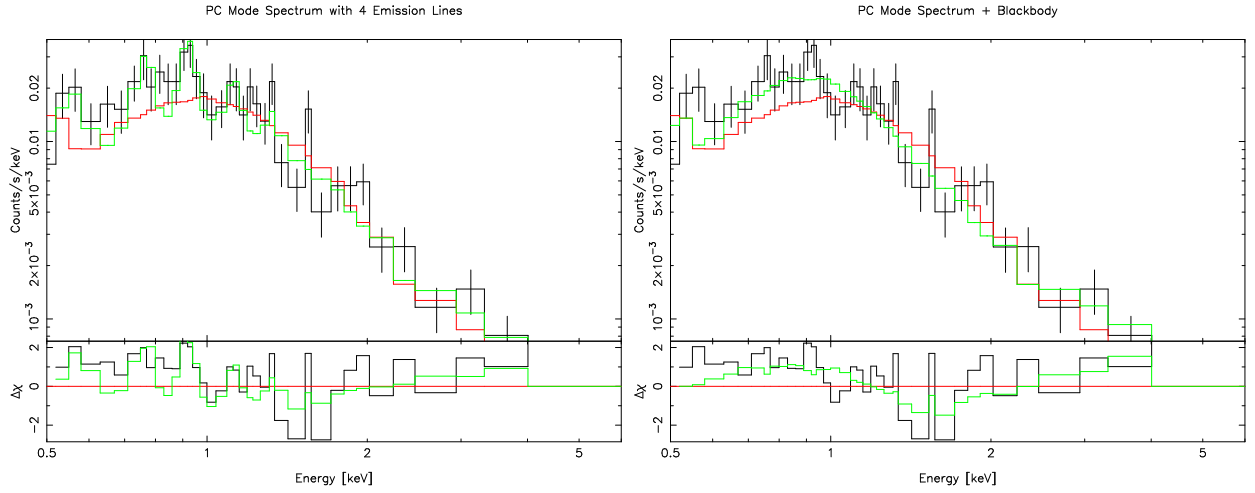


Fig. 12.— (A) During the GRB 050714B flare at  $t \sim 400$ s, emission lines at 0.56, 0.76, 0.91, and 1.12 keV (green curve), possibly associated with Si XIV, S XVI, Ar XVIII, and Ca XX at  $z = 2.66$ , improve the power-law model fit (red curve) at  $4.2\sigma$  significance (Table 7). (B) The power-law fit is also improved significantly with the inclusion of a blackbody (Table 7). The residuals panels in each plot show how the additional model components (green curves) fit the power-law continuum model residuals (black curves).

Comparing the hypothesis of emission lines to that of a blackbody (in addition to a non-thermal continuum) for GRB 050714B, we find that this event is a compelling line emission candidate. The power-law plus line model yields an excellent fit ( $\chi^2/\nu = 41.69/27$ ). However, this is little improvement over the simpler power-law plus blackbody model ( $\chi^2/\nu = 48.64/33$ ). The better fit of the MEKAL plasma model ( $\chi^2/\nu = 44.48/33$ ) for the same number of degrees of freedom appears to reinforce the line emission hypothesis.

#### 4.4. Detections in the Dyadically Grouped, > 500 Count Spectra

The sample of spectra under study is roughly doubled when we consider the additional spectra formed by dyadically grouping the  $\sim 500$  count spectra into more fully-exposed spectra containing  $> 500$  counts. We observe that the inferred line significance is clearly a function of the number of counts within the spectrum, with the more fully exposed spectra showing a higher probability of false trigger. The median significance (from the LRT) for 1-5 emission lines for the full sample is  $1.71\sigma$ . The lower and upper quartiles are  $1.21\sigma$  and  $2.23\sigma$ , respectively, implying a limit of  $5.3\sigma$  for a strong outlier. We find that only 3 bursts exhibit spectra with line triggers at the  $> 5\sigma$  level: GRBs 060218, 060202, 050822. The maximal significances are  $20.6\sigma$  ( $t = 160\text{s}-2.8$  ksec; 27,620 cts),  $6.5\sigma$  ( $t = 150\text{s}-1$  ksec; 27,620 cts), and  $5.2\sigma$  ( $t = 482.9 - 525.5\text{s}$ ; 1050 cts), respectively. GRBs 060218 and 050822 are discussed in detail above. Here, we briefly present the GRB 060202 spectrum.

The WT mode data during the first 1 ksec of GRB 060202 show two temporal declines separated by a plateau, with mild spectral evolution (Figure 14) then and afterward. The spectrum in the 0.6-10 keV band from 150s to 1ksec after the burst is unacceptably fit by a blackbody model ( $\chi^2/\nu = 2511.64/507$ ). Less poor is the absorbed power-law model fit ( $\chi^2/\nu = 644.54/507$ ), with the following best-fit parameters:  $N_H = (5.0 \pm 0.1) \times 10^{21} \text{ cm}^{-2}$  (significantly in excess of the Galactic column:  $N_{H,\text{Galactic}} = 5 \times 10^{20} \text{ cm}^{-2}$ ; Dickey & Lockman 1990),  $f = (2.04 \pm 0.02) \times 10^{-9} \text{ erg cm}^{-2} \text{ s}^{-1}$  [0.5-10 keV], and  $\Gamma = 2.32 \pm 0.02$ . Consistent values are reported by Morris et al. (2006). The fit is improved at  $6.5\sigma$  significance with the inclusion of 5 emission lines (Figure 14;  $\Delta\chi^2 = 69.06$ , for 10 additional degrees of freedom). The best fit line energies are:  $0.9 \pm 0.03$ ,  $1.01 \pm 0.03$ ,  $1.12 \pm 0.07$ ,  $4.7 \pm 0.07$ , and  $(1.19 \pm 0.04)$  keV. The line equivalent widths are  $17 \pm 3$ ,  $17 \pm 2$ ,  $17 \pm 2$ ,  $50 \pm 15$ , and  $10 \pm 2$  eV, respectively. The line luminosities are  $1.23 \pm 0.01$ ,  $1.4 \pm 0.1$ ,  $1.6 \pm 0.1$ ,  $0.5 \pm 0.2$ , and  $(0.9 \pm 0.1) \times 10^{-11} \text{ erg cm}^{-2} \text{ s}^{-1}$ , respectively.

From Keck optical spectroscopy, we have determined that the host galaxy redshift is  $z = 0.783$ . The X-ray lines can be indentified with Al XIII, Si XIII, Si XIV, Ni XXVIII, and S XV, respectively. In an initial draft of this paper, we had guessed  $z = 0.4$  for this event. Although the prediction was not borne out in detail, the complex of X-ray lines near 1 keV did correctly indicate a moderately low  $z$ . No lines are detected after 1 ksec at the  $> 2.5\sigma$  significance level. At the  $3\sigma$  level, the line luminosities are below  $1.6 \times 10^{-11} \text{ erg cm}^{-2} \text{ s}^{-1}$  and the equivalent widths are below 300 eV.

Alternatively, we can model the soft component by adding a blackbody with  $kT = 0.18 \pm 0.02$  keV (observer frame) and luminosity  $(7.4 \pm 2.4) \times 10^{-10} \text{ erg cm}^{-2} \text{ s}^{-1}$ , implying a radius  $(3.0 \pm 0.8) \times 10^{12} \text{ cm}$  (Equation 1). The reduced  $\chi^2$  is marginally lower than for the power-law plus lines model ( $\chi^2/\nu = 570.68/505$ ). The absorption is  $N_H = (5.9 \pm 0.3) \times 10^{21}$

$\text{cm}^{-2}$ , and the power-law model parameters are  $f = (1.8 \pm 0.1) \times 10^{-9} \text{ erg cm}^{-2} \text{ s}^{-1}$  [0.5-10 keV], and  $\Gamma = 2.20 \pm 0.04$ . The thermal component can also be modeled by a MEKAL plasma. However, the implied abundances are zero, indicating that the data prefer an additional continuum (rather than discrete) component.

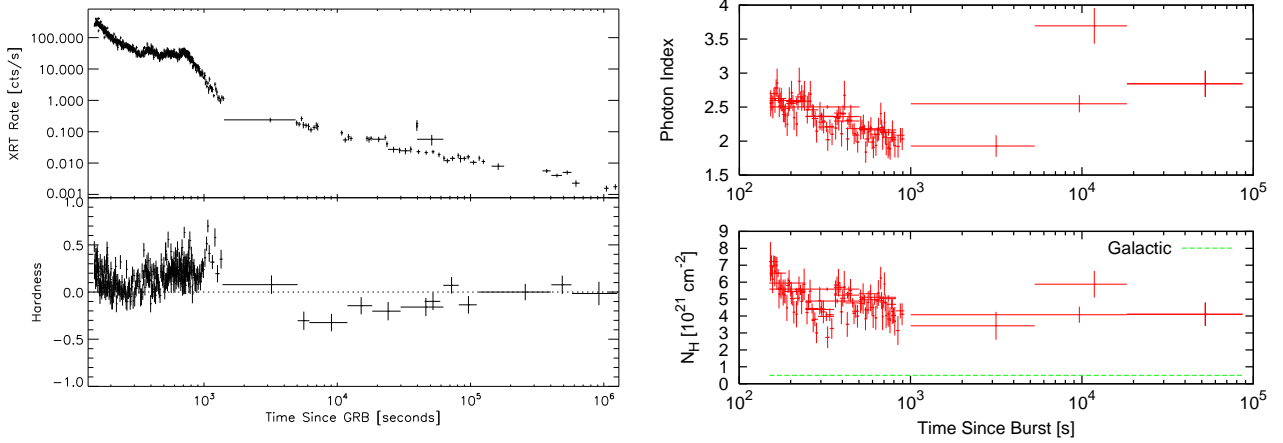


Fig. 13.— (A) The X-ray light curve and hardness plot for GRB 060202. (B) The absorbed power-law model fits.

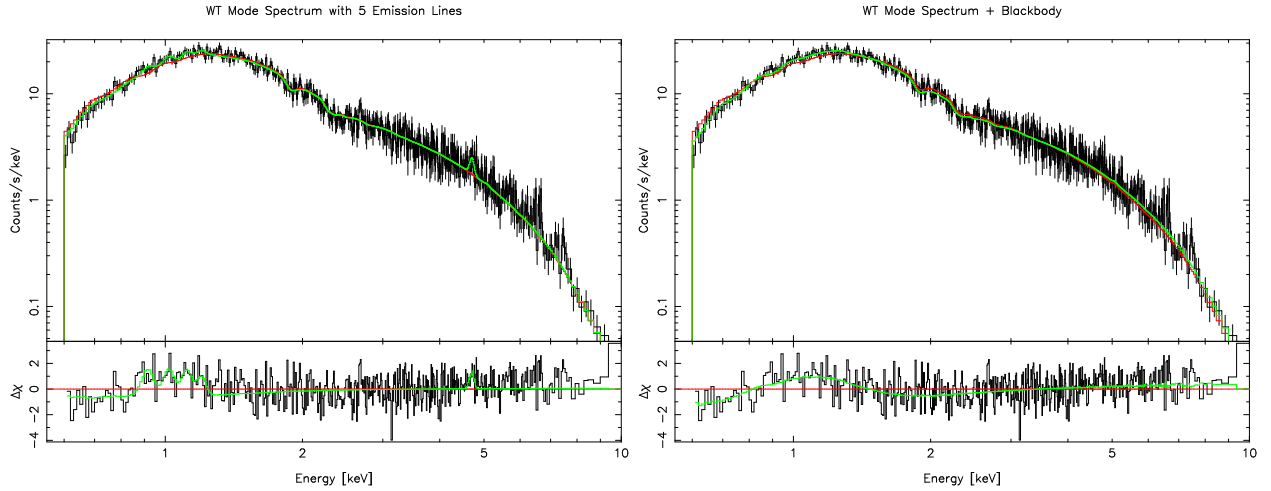


Fig. 14.— (A) The absorbed power-law model fit (red curve) to the WT mode data 150 to 1000s after GRB 060202 is improved significantly with the addition of 5 emission lines (green curve) at 0.9, 1.01, 1.12, 1.19, and 4.7 keV, possibly associated with Al XIII, Si XIII, Si XIV, Ni XXVIII, and S XV at  $z = 0.783$ . (B) A slightly better fit is found by adding a blackbody to the powerlaw. The residuals panels in each plot show how the additional model components (green curves) fit the power-law continuum model residuals (black curves).

Comparing the hypothesis of emission lines to that of a blackbody (in addition to a non-thermal continuum) for GRB 060602, we find that the blackbody model provides a better fit ( $\chi^2/\nu = 570.68/505$ ) than the more complex power-law plus lines model ( $\chi^2/\nu = 575.45/497$ ).

## 5. Discussion

### 5.1. The Spectra of Other Bright Flares

Given the detection of soft X-ray components in two bright flares, it is possible that a correlation may exist between this emission and the X-ray flaring. To explore further this possibility, we extract and fit spectra by hand to the integrated counts of 19 bright (peak count rate  $> 10$  cts/s) flares (Table 8). Because a blackbody model provides a poor fit to each spectrum, we present only the power-law model fits (Table 8). The  $\Gamma$  values for GRBs 050714B and 050228 stand out from the other values, most of which are  $\Gamma \sim 2$ . (There is also one hard outlier, GRB 050820, with  $\Gamma = 0.99 \pm 0.05$ .) We therefore conclude that these very soft spectra are uncommon in the flares.

A few of the flares, in addition to those discussed above, exhibit marginal significance ( $> 3\sigma$ ) evidence for lines on top of their non-thermal spectra (Table 9): GRBs 050502b, 051117A (during two flares), 060124 (first flare, with weak detections in the next). For GRB 060124 at  $z = 2.296$  (Prochaska et al. 2006), there is a possible Fe XXVI line near 1.9 keV and several lines at higher energies possibly associated with recombination of Fe-group elements. Although no redshift is known for GRB 050502B, the lines may also be associated with the Fe group elements: 1.44 keV—Fe XXVI, 1.69 keV—Ni XXVII, 4.48 keV—?, 2.14 keV—Fe ionization? One possible association for the lines in GRB 051117A at energies  $\sim 1.8, 2.8, 0.6, 1.4, 0.9,$  and  $1.1$  keV, is with H- or He-like Ca, Fe, Ar, Ne, Si, and S, respectively, at  $z = 1.2$ . We expect  $\sim 1$  trigger at  $\gtrsim 3\sigma$  in 22 trials. The actual number of triggers (6) suggests a modest increase in the line emission probability during the bright flaring episodes relative to the quiescent periods (e.g., Figure 3).

### 5.2. Blackbody Emission: Shock Breakout Through the Progenitor Star?

The optical/IR emission from GRB 060218 has yielded unequivocal evidence for an underlying type-Ic supernova—SN 2006aj (Mirabal et al. 2006; Sollerman et al. 2006; Modjaz et al. 2006). It has been suggested recently (Campana et al. 2006) that the unusual early X-ray emission is due to the propagation of a radiation dominated shock through a wind or H en-

velope surrounding the progenitor star. In this picture, the early X-ray light curve is broad, then rapidly declining, due to light travel time effects across an aspherical shock shell of thickness  $\sim R/\Gamma c \sim 300s$ .

The shock can be due to the GRB itself (Tan, Matzner, & McKee 2001; Colgate 1974) or due to mildly relativistic material expected to form and surround the GRB jet as it punches through the He core of the progenitor star at  $R_{\text{He}} \lesssim 10^{11}$  cm (Mészáros & Rees 2001; Ramirez-Ruiz, Celotti, & Rees 2002). After the shock punches through an optically thick layer around the He core and interacts with the envelope, it leaves behind an expanding photosphere. The radius at which the light is able to escape the photosphere around a carbon-rich, Wolf-Rayet star is  $R_p = 1.5 \times 10^{12} \frac{\dot{M}_{-4}}{v_{w,8}}$  cm (Tan, Matzner, & McKee 2001). The scatter in observed mass loss rates ( $\dot{M}_{-4}$  in units of  $10^{-4} M_{\odot} \text{ yr}^{-1}$ ) and wind velocities ( $v_{w,8}$  in units of  $10^8$  cm/s) is  $\sim 1$  dex (Koesterke & Hamann 1995) and could lead to a  $\sim \pm 1$  dex range in  $R_p$ . Due to the energy input ( $\sim 10^{51}$  erg) the expected photospheric blackbody temperature is  $\sim 0.3$  keV.

In the course of our line search, we find spectra from 3 other events which are soft and well fit by models containing a blackbody. Aside from no clear detection in the UV (Gronwall et al. 2005; Page et al. 2005b; Blustin et al. 2006), these detections are similar to GRB 060218 in a number of ways. In each case the observation epoch is  $\sim 1$  ksec, and the blackbody radii are  $R_{\text{BB}} \sim 10^{12} - 10^{13}$  cm. We also find similar temperatures ( $\sim 0.1 - 0.5$  keV) in each case, which appear to decrease in time mildly. In all cases, the emission is transient. The  $R_{\text{BB}}/c$  are similar to the light travel time from the GRB to the observation epoch, which would imply a simultaneous GRB and SN in either scenario discussed above. The radii are at least 2 orders of magnitude smaller than the distance expected for the highly relativistic ( $\Gamma \sim 10$ ) external shock at the observation epoch, ruling out an association with the external shock.

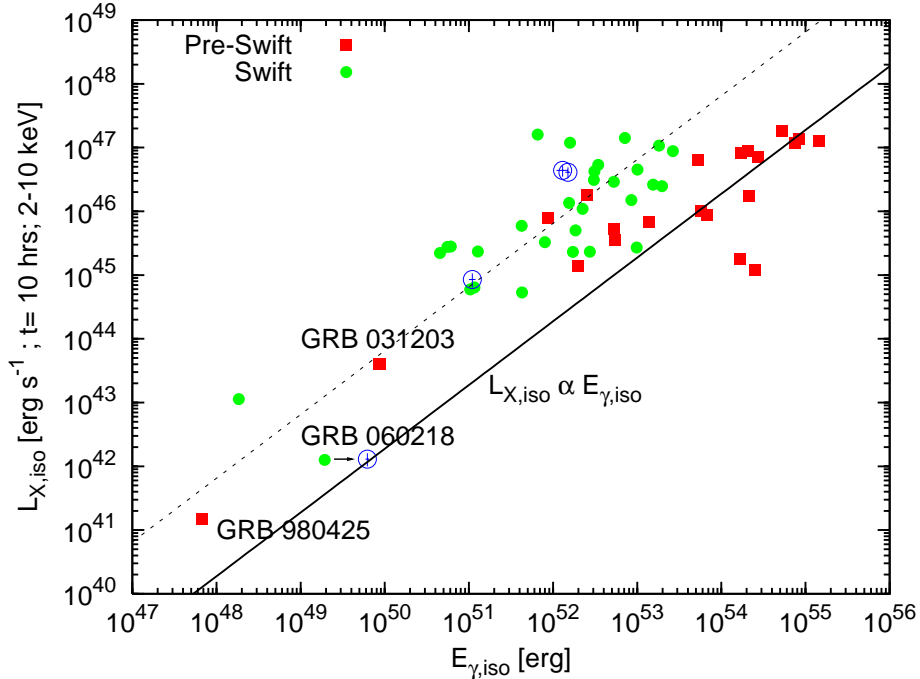


Fig. 15.— The isotropic X-ray luminosity at  $t = 10$  hours in the host frame versus the isotropic prompt energy release in  $\gamma$ -ray’s. Fluence data for *Swift* (typically in the 15-150 keV band) are taken from the table at [http://swift.gsfc.nasa.gov/docs/swift/archive/grb\\_table](http://swift.gsfc.nasa.gov/docs/swift/archive/grb_table), and these are translated to  $E_{\gamma,iso}$  by multiplying by  $4\pi D_L^2/(1+z)$  only. The bursts studied here are shown encircled in blue. The parallel track set by the *Swift* bursts relative to bursts prior to *Swift* likely reflects only the narrow BAT band pass and our non-application of a k-correction, which apparently leads to systematic underestimates of  $E_{\gamma,iso}$ . Note the shift in  $E_{\gamma,iso}$  for GRB 060218 depending on whether we use the tabulated value or the more carefully calculated value from Campana et al. (2006).

An additional clue to the mechanism which produces the soft component may come from a simple comparison of the GRB and shock kinetic energies. We can infer the shock kinetic energy using the X-ray afterglow luminosity at  $t = 10$  hours in the host frame, which is expected to scale linearly with the shock energy due to an independence on the density and a mild dependence on the shock microphysical parameters (e.g., Berger, Kulkarni, & Frail 2003). GRB 060218, like GRB 980425/SN 1998bw and GRB 031203/SN 2003lw, is found to track other GRBs from *Swift* and previous missions (Figure 15), implying a roughly similar efficiency for the conversion of shock kinetic energy into  $\gamma$ -ray’s, but with a substantial sub-luminosity evident in both quantities. The other bursts discussed above also follow the trend  $L_{X,iso} \propto E_{\gamma,iso}$ .

On the other hand, using the fact that the duration of the photospheric expansion phase

appears to be  $\sim 10^2 - 10^3$ s for each burst, we can estimate the ratio of blackbody fluence to prompt GRB fluence (Table 10). The prompt  $\gamma$ -ray energy release for GRBs 060202, 050822, and 050714B is  $S_\gamma = 2.4 \pm 0.2$  (Hullinger et al. 2006),  $3.4 \pm 0.3$  (Hullinger et al. 2005), and  $(0.7 \pm 0.1) \times 10^{-6}$  erg cm $^{-2}$  (Tueller et al. 2005), respectively, in the 15-150 keV band. The ratios are found to be:  $0.3 \pm 0.1$ ,  $0.03 \pm 0.01$ , and  $0.2 \pm 0.1$ , respectively. The ratio value for GRB 060218 is  $4 \pm 1$ . The soft fluence clearly correlates with the prompt  $\gamma$ -ray and shock emission. The large dispersion over more than two orders of magnitude could be explained by the diversity of observed progenitor wind outflows and the strong dependence of the available energy  $E$  on the mass loss history:  $E \approx \Gamma^2 R_p \frac{\dot{M} c^2}{v_w} \propto \left(\frac{\dot{M}}{v_w}\right)^2$  (Tan, Matzner, & McKee 2001).

Because wide variations in the thermal energy release apparently do not alter the  $L_{X,\text{iso}} \propto E_{\gamma,\text{iso}}$  relation, we conclude that the soft component is more likely to have been produced by the cocoon surrounding the GRB jet as it escape the progenitor He core than by the GRB jet itself. A radiation dominated cocoon is not expected to appreciably affect the standard internal shocks or afterglow emission (Ramirez-Ruiz, Celotti, & Rees 2002). On the issue of the faintness of GRB 060218, Fan, Piran, & Xu (2006) discuss the possibility that GRB 060218 was an almost “failed GRB,” with a large fraction of the GRB energy not making it out of the progenitor star and winding up as thermal photons in the cocoon.

One additional insight which comes from the extreme proximity of GRB 060218, it’s sub-luminous  $\gamma$ -ray emission, and the relative faintness of the soft X-ray components in 3 other bursts is that this emission could be relatively common. Bursts like GRB 060218, where the spectrum is dominated by the soft component could outnumber normal GRBs 100 to 1. It may be a selection effect that the blackbody radiation happens to peak where the detector response is also maximal at  $E \approx 5kT \sim 0.5 - 2$  keV for each of these events; soft or harder spectra due to breakout at larger or smaller radii, respectively, may also occur.

### 5.3. Constraints on the Line Emission Mechanisms

In the previous section we discussed the soft X-ray emission in terms of the blackbody fits. For 3 of the 4 bursts in Section 4, the data appear to be fit better with an emission line model. Clear line associations are possible for GRB 060218 and possible association are presented for the other bursts lacking redshift measurement. For two of the bursts, the line component is well fit by a thermal plasma model containing only two parameters (temperature and normalization). Because, the continuum under the lines is dominated by a power-law, the emitting plasmas may well not be in thermal equilibrium. Lazzati (2003) has discussed the relative unlikelihood that GRB X-ray lines could be due to thermal plasmas.



For simplicity in fitting, however, the MEKAL code generates approximately correct line locations and sensible flux ratios for a broad range of astrophysically abundant elements. The code has been shown to produce similar lines as from photo-ionization models (e.g., Watson et al. 2003), at the level of spectral resolution appropriate to *Swift* XRT data. In the case of GRB 050822, the MEKAL model cannot produce the closely spaced lines, and this may argue for a non-equilibrium ionization state, for two plasmas with differing ionization states, or for plasmas moving at different speeds ( $\lesssim 0.1c$ ) relative to the observer.

In none of the cases do we detect lone, statistically significant emission lines. Rather, we find sets of lines, typically fairly closely spaced in energy, which we associate with ionized light metals or with L-shell transitions in Fe (GRB 060218). The line sets we find are perhaps most similar to the light metal lines (Reeves et al. 2002; Watson et al. 2003) and soft, possibly thermal excesses (Watson et al. 2002) found in *XMM* data. A detection of such lines has been claimed for *Chandra* as well (Butler et al. 2003).

Figure 16, adapted from Butler, et al. (2005b), displays the line triggers in the context of lines claimed from previous missions. For comparison and for estimation of upper limits for the  $\sim 90\%$  of spectra not showing significant evidence for lines, Figure 17 displays equivalent width values versus time for marginal detections in the full dataset of *Swift* bursts with measured redshift. It is difficult to use the triggers or upper limits to rule on the reality of the historic lines, because there are few well-exposed XRT spectra at  $t \gtrsim 0.1$  day. However, observations with *Chandra* place stringent limits on the late-time lines (down arrows in Figure 16; Butler, et al. 2005b). The upper limits from the non-detections ( $EW \lesssim 1$  keV at  $t < 0.1$  day) in the *Swift* XRT sample are roughly consistent with the detections.

The most striking feature of the triggers is that the possible lines are emitted at dramatically earlier times ( $t < 0.1$  day) than in previous cases. Prior to *Swift*, it was suspected that GRB lines would be very difficult to form at early times (aside from exotic possibilities suggested by, e.g., Gou, Mészáros, & Kallman 2004) due to the overwhelming flux from the bright X-ray afterglow. The solid lines in Figure 16 show the rapid decrease expected at early times for two photo-ionization models (Ballantyne & Ramirez-Ruiz 2001; Butler, et al. 2005b). The data from GRB 060218 may roughly follow this expectation, but the other data likely do not.

One of the big surprises from *Swift* was the departure of the early X-ray afterglow light curves from late time extrapolations (early flaring, anomalously flat and rapidly decaying early light curves, e.g., Nousek et al. 2006; Zhang et al. 2006). In some cases, the afterglows are fainter at early times ( $t \sim 10^2 - 10^4$ s) than previously suspected. The explanation for why we see lines possibly correlated with flare emission may simply be that both depend on similar circumstances—non overpowering external shock emission—for their detection.

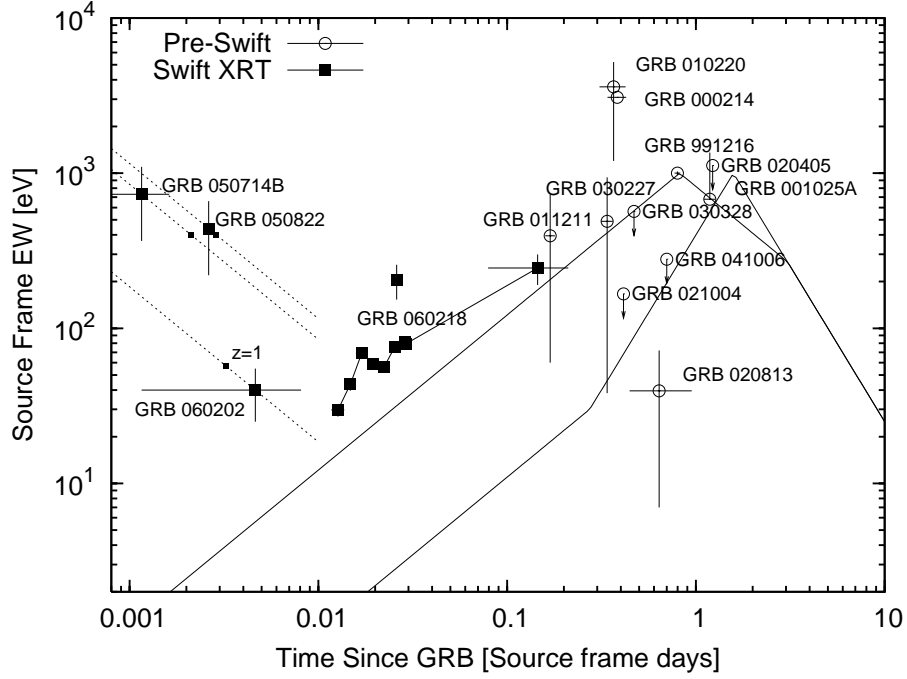


Fig. 16.— Equivalent width  $EW$  versus time in the source frame, adapted from Butler, et al. (2005b). The four bursts studied here are marked as solid squares. The dotted curves show how the point for GRBs 060202, 050822, and 050714B move as the redshift is varied (small solid squares mark  $z = 1$  for each burst). A number of points are measured for GRB 060218 in the  $\sim 16,000$  cts spectra (connected by a line), with one possible larger  $EW$  value from the  $\sim 500$  cts spectra (Section 4). Previous detections and upper limits are marked with open circles and labeled. The solid curves represent photoionization models from Ballantyne & Ramirez-Ruiz (2001), explained in more detail in Butler, et al. (2005b).

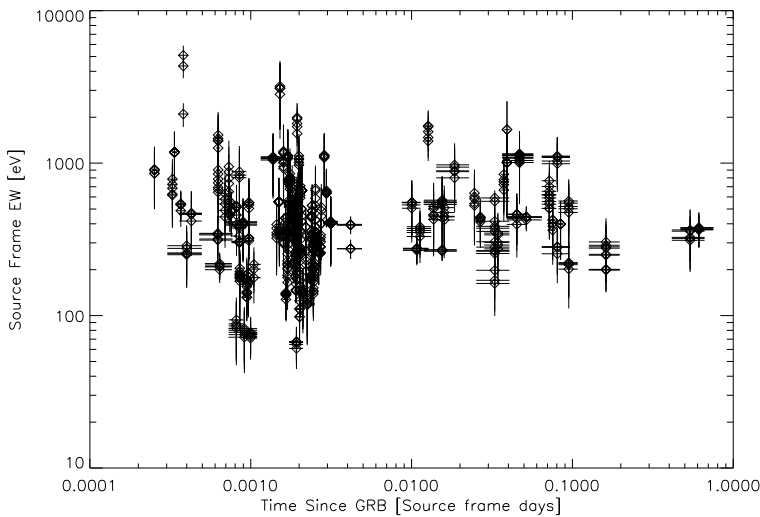


Fig. 17.— Equivalent width  $EW$  versus time in the source frame for all (marginal) triggers at  $> 2\sigma$  significance for 28 *Swift* XRT afterglows with measured redshifts, excluding GRB 060218. Redshifts are taken from the GCN. We restrict to only the spectra observed with exposures  $\delta t < t_{\text{mean}}/2$ . Ninety percent of the  $EW$  values below 0.1, 0.01, or 0.01 days have  $EW < 1$  keV. There are few spectra (3% of the sample) at times  $> 0.1$  day in the source frame.

Both the trigger times and apparent transient nature of the lines limit the distance from the progenitor:

$$R < \frac{ct_{\text{obs}}}{1+z} \frac{1}{1-\cos(\theta)} \lesssim 10^{13} \text{ cm}, \quad (2)$$

where  $\theta$  is the angle between the line emitting material and the line of sight (e.g., Vietri et al. 2001). This implicates models from the so called “nearby reprocessor” class, whereby the lines are produced by a long-lasting central engine (Rees & Mészáros 2000) or with the help of magnetic field energy stored in the plasma bubble discussed above (Mészáros & Rees 2001). The small distances from the progenitor favor one-step “hypernova” explosions (e.g., Woosley 1993; Paczyński 1998) and disfavor a SN occurring prior to the GRB (e.g, Vietri & Stella 1998). For the plasma bubble, a possibly large magnetic field ( $\sim 10^5$  Gauss) can be entrained and carried with the flow, both maintaining clumps of matter in the flow and allowing for synchrotron irradiation of the clumps (Mészáros & Rees 2001). Or the lines could be generated by reflection from cold matter in the funnel wall carved out by the GRB jet from the progenitor (e.g., Kallman, Mészáros, & Rees 2003).

The chemical species we infer point to ionization parameters  $\xi = L_x/nR^2 \lesssim 10^2$  (Lazzati, Ramirez-Ruiz, & Rees 2002). If the continuum luminosities  $L_X$  we measure are directly responsible for the lines, this implies a density  $n \sim 10^{18} \text{ cm}^{-3}$  (GRB 060218) -  $10^{21}$

$\text{cm}^{-3}$  (GRB 050822). Because the largest densities expected in the nearby reprocessor scenario are  $\gtrsim 10^{17} \text{ cm}^{-3}$  (Rees & Mészáros 2000; Mészáros & Rees 2001), a small fraction of the observed continuum ( $\sim 0.01 - 10\%$ ) must be powering the lines.

#### 5.4. Systematic Uncertainties in the XRT Response

Calibration efforts for the XRT spectral response are ongoing<sup>4</sup>. The quality of the current response matrices at low energy could have an important impact on the explanation for the soft excesses, particularly on the possibility of X-ray lines. Here we address a number of concerns raised by the XRT team (D. Burrows, private communication). This can be done quantitatively now due to the release of the v008 response files. The v008 files allow for the fitting of both the PC and WT mode data in the full 0.3-10 keV band, with the requirement of a small (3%) systematic error component.

We have rerun the analysis using the v008 response files and including the systematic errors. For the 0.3-10 keV band, we find consistent distributions for the continuum fit parameters and continuum fit goodnesses (Figure 2) and line trigger significances (Figure 3) for the PC mode data. The distributions for continuum fit parameters for the WT mode data are also consistent. There is, however, a dramatic increase in the number of line triggers for the WT mode data for the well exposed spectra of 5 bright afterglows (GRBs 050502B, 060124, 060202, 060210, 060211A). The line triggers fall near 0.5 keV and are clearly due to a dip near the O-K edge at 0.532 keV, which can also be seen in Figures 12 and 8 for the spectra for GRBs 050714B and 060218. The XRT team argues that the dip—also seen in calibration observations of the Crab, 3C273, and H1426+428—is due to a gain offset  $\lesssim 80$  eV, which occurs occasionally for WT mode data due to a problem with the bias subtraction. (It may also occur for the PC mode data, possibly due to illumination by the bright Earth.) Because we observe the magnitude of the dip to be proportional to the absorbing column  $N_H$  (hence to the depth of the O-K edge), we agree with this explanation. This observation rules out the more pernicious possibility of a significant problem with the response files below 0.6 keV. Also, we note that the spectra for the 5 WT mode bursts showing the dip can be adequately fit by absorbed power-laws if we also fit for the gain offset.

One possible additional concern with 3 of the 4 bursts with significant line triggers is that the triggers appear to occur near the same observed energies (i.e., at  $\sim 100$  eV intervals near 0.8, 0.9, 1.0 keV, etc), possibly indicating an instrumental origin. From simulations, we note that line-like residuals due to the gain offset are unimportant  $\lesssim 10\%$  effects in this

---

<sup>4</sup>[http://swift.gsfc.nasa.gov/docs/swift/analysis/xrt\\_digest.html](http://swift.gsfc.nasa.gov/docs/swift/analysis/xrt_digest.html)

energy range. (There can be narrow residuals near the Si-K edge at 1.839 keV at the  $\sim 20\%$  level, however). Also, fitting for the gain, we find that the inferred trigger significances do not change. We, therefore, rule out the possibility that the instrumental effect of the gain offset produces the line triggers. Reinforcing this conclusion, a large number spectra with comparable source intensities to those with possible line detection are well fit by simple power-laws (Figures 2A, 3). However, we cannot entirely rule out the possibility that the low spectral resolution of the detector could allow for acceptable fits of an additive continuum component by closely spaced lines. This possibility is strengthened by the degradation of the of spectral resolution (from 0.08 keV at launch to  $\sim 0.1$  keV in late 2006) due to radiation damage, an effect which is not treated in the v007 or v008 response files.

## 6. Conclusions

We have conducted a thorough and blind search for emission lines through nearly 0.4 years of X-ray afterglow data accumulated by the *Swift* XRT. The majority of spectra (90%) are well fit by absorbed power-law models, but significant outliers to the population at the 5-10% level exist and have anomalously soft, possibly thermal spectra. Four bursts are singled out as possibly exhibiting 2-5 emission lines: GRBs 060218, 060202, 050822, and 050714B. Removed from the sample, line triggers in the spectra of the other bursts are consistent with Poisson fluctuations in the continua.

The most significant soft component detections in the full data set of  $\sim 2000$  spectra correspond to GRB 060218/SN 2006aj, with line triggers ranging from  $4\sigma$  to  $\sim 20\sigma$ . A thermal plasma model fit to the data indicates that the emission may be primarily due to L-shell transitions of Fe at  $\sim$  solar abundance. The possible line emission occurs near  $t \sim 1$  ksec, with a similar observed duration, indicating emitting material at  $R \sim 10^{13}$  cm. We suggest that the emission is due to the mildly relativistic cocoon of matter surrounding the GRB jet as it penetrates and exits the surface of the progenitor star. We associate the ( $> 4\sigma$  significant) line emission from 3 other events lacking redshifts with K-shell transitions in light metals. The lines in these bursts point to emission at similar distances, possibly at similar densities  $\sim 10^{17}$  cm $^{-3}$ , and possibly subject to similar fluxes of ionizing radiation.

As an alternate possibility—difficult to distinguish with the broad XRT spectral resolution ( $\sim 80$  eV FWHM at 1 keV)—we successfully model the spectra using blackbody continuum components in addition to power-laws. With radii (again  $\sim 10^{12} - 10^{13}$  cm) and temperatures ( $\sim 0.1 - 0.5$  keV) implied by the fits, the possibility exists that the emission is continuous rather than discrete and possibly again due break out of the GRB shock or plasma cocoon from the progenitor star. We find that the energetics of the GRB and its

shock, inferred from the 4 events where breakout emission may be present, point toward the cocoon as the likely source of the soft component. Bursts faint in  $\gamma$ -rays with spectra dominated by a soft X-ray flux possibly due to the shock breakout may outnumber classical GRBs 100-1. Typically, the breakout flux would be faint or dominated by the external shock afterglow emission. The degeneracy between continuum and discrete emission components could possibly be lifted if redshifts are determined for the events discussed above or if redshifts are measured for bursts detected by *Swift* in the coming years with soft X-ray anomalies.

N. Butler gratefully acknowledges support from a Townes Fellowship at U. C. Berkeley Space Sciences Laboratory and partial support from J. Bloom and A. Filippenko. Special thanks to J. Bloom and the U. C. Berkeley GRB team for comments on the manuscript and several useful conversations. Additional thanks to the *Swift* team for impressively rapid public release and analysis of the XRT data.

## REFERENCES

- Antonelli, L. A., et al. 2000, ApJ, 545, L39
- Ballantyne, D. R., & Ramirez-Ruiz, E. 2001, ApJ, 559, L83
- Berger, E., Kulkarni, S. R., & Frail, D. A. 2003, ApJ, 590, 379
- Blustin, A. J., et al. 2006, GCN #4633
- Butler, N. R., et al. 2003, ApJ, 597, 1010
- Butler, N. R., et al. 2005a, ApJ, 627, L9
- Butler, N. R., et al. 2005b, ApJ, 629, 908
- Campana, S., et al. 2006, Submitted to Nature, astro-ph/0603279
- Colgate, S. A. 1974, ApJ, 187, 333
- Costa, E., et al. 1999, A&A Suppl. 138, 425
- Cusumano, G., et al. 2006a, GCN #4775
- Cusumano, G., et al. 2006b, GCN #4786

- Devore, J., L., Probability and Statistics for Engineering and Sciences, (4th ed.; Belmont, CA: Wadsworth)
- Dickey, J. M., & Lockman, F. J. 1990 ARAA, 28, 215
- Fan, Y., Piran, T., & Xu, D. 2006, astro-ph/0604016
- Godet, O., et al. 2005, GCN #3873
- Gou, L. J., Mészáros, P., & Kallman, T. R. 2005, ApJ, 624, 889
- Gronwall, C., et al. 2005, GCN #3620
- Hullinger, D., et al. 2005, GCN #3856
- Hullinger, D., et al. 2006, GCN #4635
- Kallman, T., Mészáros, P., & Rees, M. J. 2003, ApJ, 593, 946
- Koesterke, L., & Hamann, W.-R. 1995, A&A, 299, 503
- Lazzati, D. 2003, A&A, 399, 913
- Lazzati, D., Campana, S., & Ghisellini, G. 1999, MNRAS, 304, L31
- Lazzati, D., Ramirez-Ruiz, E., & Rees, M. J. 2002, ApJ, 572, L57
- Mészáros, P., & Rees, M. J. 2001, ApJ, 556, L37
- Mewe, R., Gronenschild, E. H. B. M., van den Oord, G. H. J. 1985, A&AS, 62, 197
- Mirabal, N., et al. 2006, astro-ph/0603686, submitted to ApJL
- Modjaz, M., et al. 2006, astro-ph/0603377, submitted to ApJL
- Morris, D., et al. 2006, GCN #4632
- Nousek, J. A., et al. 2006, astro-ph/0508332, to appear in ApJ
- Paczyński, B. 1998, ApJ, 494, L45
- Page, K., et al. 2005a, GCN #3618
- Page, M. J., et al. 2005b, GCN #3859
- Piro, L., et al. 1999, A&AS, 138, 431

- Piro, L., et al. 2000, *Science*, 290, 955
- Prochaska, J. X., et al. 2005, GCN #3332
- Prochaska, J. X., et al. 2006, GCN #4593
- Protassov, R., et al. 2002, *ApJ*, 571, 545
- Ramirez-Ruiz, E., Celotti, A., & Rees, M. 2002, *MNRAS*, 337, 1349
- Rees, M. J., & Mészáros, P. 2000, *ApJ*, 545, L73
- Reeves, J. N., et al. 2002, *Nature*, 415, 512
- Rutledge, R., & Sako, M. 2003, *MNRAS*, 339, 600
- Sako, M., Harrison, F., & Rutledge, R. 2005, *ApJ*, 623, 973S
- Sollerman, J., et al. 2006, astro-ph/0603495, submitted to *A&A*
- Tan, J. C., Matzner, C. D., & McKee, C. F. 2001, *ApJ*, 551, 946
- Tueller, J., et al. 2005, GCN #3615
- Vietri, M., et al. 2001, *ApJ*, 550, L43
- Vietri, M., & Stella, L. 1998, *ApJ*, 507, L45
- Watson, D., et al. 2002, *A&A*, 393, L1
- Watson, D., et al. 2003, *ApJ*, 595, L29
- Woosley, S. E. 1993, *ApJ*, 405, 273
- Yaqoob, T. 1998, *ApJ*, 500, 893
- Yoshida, A., et al. 1999, *A&AS*, 138 433
- Zhang, B., et al. 2005, astro-ph/0508321



Table 1: Time-resolved Spectroscopy in  $\sim 16,000$  cts Spectra for GRB 060218

#	Time (ksec)	BB Flux	$kT$ (keV)	$\chi^2/\nu$	PL Flux	$\Gamma$	$N_H$	$\chi^2/\nu$
WT Mode								
1	0.161-0.475	211.00 $\pm$ 1.72	0.94 $\pm$ 0.01	1718.48/535	372.40 $\pm$ 3.61	1.54 $\pm$ 0.02	3.97 $\pm$ 0.10	595.99/535
		124.30 $\pm$ 53.90	0.18	+	324.80 $\pm$ 7.37	1.50 $\pm$ 0.04	5.73 $\pm$ 0.54	537.20/530
2	0.475-0.688	40.28 $\pm$ 2.71	0.98 $\pm$ 0.01	1662.32/549	571.20 $\pm$ 5.47	1.46 $\pm$ 0.02	3.72 $\pm$ 0.10	573.38/549
		147.18 $\pm$ 70.86	0.17	+	496.20 $\pm$ 10.19	1.44 $\pm$ 0.04	5.31 $\pm$ 0.54	535.00/544
3	0.688-0.872	45.30 $\pm$ 3.06	0.95 $\pm$ 0.01	1724.45/529	661.90 $\pm$ 6.35	1.57 $\pm$ 0.02	4.11 $\pm$ 0.10	629.89/529
		340.95 $\pm$ 152.11	0.16	+	591.50 $\pm$ 13.57	1.55 $\pm$ 0.04	6.21 $\pm$ 0.56	537.88/524
4	0.872-1.046	48.00 $\pm$ 3.22	0.92 $\pm$ 0.01	1499.49/522	689.20 $\pm$ 6.76	1.62 $\pm$ 0.02	3.97 $\pm$ 0.10	640.10/522
		761.00 $\pm$ 348.78	0.13	+	659.20 $\pm$ 16.94	1.71 $\pm$ 0.04	6.85 $\pm$ 0.59	603.46/517
5	1.046-1.223	44.07 $\pm$ 2.96	0.87 $\pm$ 0.01	1444.86/500	670.20 $\pm$ 6.87	1.80 $\pm$ 0.02	4.49 $\pm$ 0.10	621.45/500
		2067.00 $\pm$ 851.39	0.12	+	691.80 $\pm$ 20.88	1.94 $\pm$ 0.04	8.26 $\pm$ 0.56	539.78/495
6	1.223-1.411	39.48 $\pm$ 2.65	0.82 $\pm$ 0.01	1486.17/493	622.80 $\pm$ 6.66	1.91 $\pm$ 0.02	4.46 $\pm$ 0.10	602.29/493
		1992.59 $\pm$ 849.83	0.12	+	652.90 $\pm$ 21.46	2.03 $\pm$ 0.04	8.04 $\pm$ 0.57	529.29/488
7	1.411-1.617	33.38 $\pm$ 2.23	0.77 $\pm$ 0.01	1419.64/470	545.10 $\pm$ 6.16	2.03 $\pm$ 0.02	4.47 $\pm$ 0.09	584.09/470
		6199.44 $\pm$ 2325.48	0.10	+	640.30 $\pm$ 22.94	2.25 $\pm$ 0.04	9.24 $\pm$ 0.50	458.65/465
8	1.617-1.851	27.12 $\pm$ 1.83	0.71 $\pm$ 0.00	1413.91/440	478.90 $\pm$ 6.18	2.23 $\pm$ 0.02	4.64 $\pm$ 0.09	566.43/440
		4650.94 $\pm$ 1842.21	0.11	+	568.40 $\pm$ 23.49	2.42 $\pm$ 0.04	8.83 $\pm$ 0.52	446.16/435
9	1.851-2.116	22.03 $\pm$ 1.48	0.64 $\pm$ 0.00	1563.68/422	406.90 $\pm$ 5.56	2.34 $\pm$ 0.02	4.33 $\pm$ 0.09	578.89/422
		4248.35 $\pm$ 1666.76	0.11	+	483.30 $\pm$ 21.47	2.50 $\pm$ 0.04	8.59 $\pm$ 0.51	442.47/417
10	2.116-2.401	18.26 $\pm$ 1.30	0.57 $\pm$ 0.00	1845.22/389	380.70 $\pm$ 6.16	2.57 $\pm$ 0.03	4.45 $\pm$ 0.09	640.99/389
		3146.32 $\pm$ 1199.94	0.11	+	417.70 $\pm$ 20.08	2.61 $\pm$ 0.05	8.10 $\pm$ 0.48	400.39/383
11	2.401-2.753	14.43 $\pm$ 0.98	0.53 $\pm$ 0.00	1791.20/371	313.00 $\pm$ 5.57	2.69 $\pm$ 0.03	4.34 $\pm$ 0.08	630.66/371
		2706.92 $\pm$ 986.90	0.11	+	337.90 $\pm$ 16.90	2.71 $\pm$ 0.05	7.88 $\pm$ 0.45	344.64/365
PC Mode								
12	5.950-2.872 Msec	0.009 $\pm$ 0.001	0.36 $\pm$ 0.02	215.47/93	0.031 $\pm$ 0.003	3.41 $\pm$ 0.13	4.39 $\pm$ 0.27	144.03/93
		0.43 $\pm$ 0.16	0.10 $\pm$ 0.01	+	0.03 $\pm$ 0.01	3.17 $\pm$ 0.24	7.33 $\pm$ 1.36	87.94/91

Notes: Column density  $N_H$  measured in units of  $10^{21}$   $\text{cm}^{-2}$ .  $N_{H,\text{Galactic}} = 1.11 \times 10^{21}$   $\text{cm}^{-2}$  (Dickey & Lockman 1990).  $N_H$  fixed at lower limit  $3.7 \times 10^{20}$   $\text{cm}^{-2}$  for pure blackbody (BB) fits. Flux measured in units of  $10^{-11}$   $\text{erg cm}^{-2} \text{s}^{-1}$ , 0.5-10 keV for the power-law (PL) and bolometric for the blackbody. Temperature measured in the source frame,  $z = 0.033$  (Mirabal et al. 2006).

Table 2: Time-resolved Line Search in  $\sim 16,000$  cts Spectra for GRB 060218

#	Time [s]	N lines	Signif.	Line Energy , Equivalent Width , Flux (keV,eV, $10^{-11}$ erg cm $^{-2}$ s $^{-1}$ )				
WT Mode								
1	0.161-0.475	0	$< 5.0\sigma$	...				
2	0.475-0.688	0	$< 5.0\sigma$	...				
3	0.688-0.872	0	$< 5.0\sigma$	...				
4	0.872-1.046	0	$< 5.0\sigma$	...				
5	1.046-1.224	5	$7.0\sigma$	(0.93,28,5.5)	(3.19,45,3.3)	(3.65,40,2.6)	(1.02,20,3.6)	(2.76,30,2.5)
6	1.224-1.411	5	$5.9\sigma$	(0.95,26,5.2)	(1.14,16,2.8)	(3.24,28,1.9)	(0.87,23,4.8)	(1.03,16,3.0)
7	1.411-1.618	5	$8.2\sigma$	(0.89,42,9.1)	(0.80,40,9.7)	(1.06,22,3.9)	(4.04,47,2.1)	(0.97,18,3.5)
8	1.618-1.851	5	$8.0\sigma$	(1.00,37,7.3)	(0.79,51,13.4)	(0.90,35,7.9)	(1.12,23,3.9)	(0.71,47,14.1)
9	1.851-2.116	5	$9.3\sigma$	(0.96,34,6.0)	(0.88,32,6.4)	(0.79,33,7.5)	(1.06,21,3.3)	(2.55,31,1.5)
10	2.116-2.401	5	$13.3\sigma$	(0.92,55,10.7)	(1.01,40,6.8)	(0.80,39,9.3)	(1.11,26,3.8)	(0.75,33,8.8)
11	2.401-2.7535	5	$14.1\sigma$	(0.90,49,8.4)	(0.99,40,5.8)	(0.78,42,9.1)	(1.12,23,2.8)	(0.85,24,4.6)
PC Mode								
12	5.950-2.872 Msec	4	$7.1\sigma$	(0.80,109,0.003)	(0.89,78,0.001)	(0.69,96,0.003)	(1.07,43,0.001)	

Table 3: Time-Integrated Spectroscopy for GRB 060218

Model	$N_H$	Norm.	$\Gamma$ or kT (keV)	$\chi^2/\nu$
WT Mode Data $t = 160\text{s}-2.8\text{ksec}$				
power-law	$3.6 \pm 0.1$	$(3.43 \pm 0.01) \times 10^{-9}$	$1.84 \pm 0.01$	1740.56/768
blackbody	$0.4 \pm 0.1$	$(1.84 \pm 0.01) \times 10^{-9}$	$0.769 \pm 0.002$	14434.53/768
power-law	$7.2 \pm 0.2$	$(3.51 \pm 0.03) \times 10^{-9}$	$1.95 \pm 0.01$	
+ blackbody		$(7.6 \pm 0.9) \times 10^{-9}$	$0.123 \pm 0.002$	1111.33/766
power-law	$4.0 \pm 0.2$	$(3.40 \pm 0.01) \times 10^{-9}$	$1.82 \pm 0.01$	
+ MEKAL		$(8.0 \pm 0.5) \times 10^{-2}$	$0.82 \pm 0.02$	1323.00/766
PC Mode Data $t = 5.9\text{ksec}-3.1\text{Msec}$				
power-law	$4.4 \pm 0.3$	$(3.1 \pm 0.3) \times 10^{-13}$	$3.4 \pm 0.1$	143.99/93
blackbody	$0.5 \pm 0.2$	$(9.0 \pm 0.4) \times 10^{-14}$	$0.36 \pm 0.02$	215.24/93
power-law	$6.9 \pm 1.3$	$(2.5 \pm 0.6) \times 10^{-13}$	$3.1 \pm 0.2$	
+ blackbody		$(2.9 \pm 0.7) \times 10^{-12}$	$0.10 \pm 0.01$	87.63/91
power-law	$5.6 \pm 0.7$	$(2.5 \pm 0.32) \times 10^{-13}$	$3.1 \pm 0.1$	
+ MEKAL		$(2.8 \pm 0.5) \times 10^{-4}$	$0.23 \pm 0.03$	66.01/91

Notes: Column density  $N_H$  measured in units of  $10^{21} \text{ cm}^{-2}$ .  $N_{H,\text{Galactic}} = 1.11 \times 10^{21} \text{ cm}^{-2}$  (Dickey & Lockman 1990). Power-law model normalization (Norm.) in units of  $\text{erg cm}^{-2} \text{ s}^{-1}$  [0.5-10 keV]. Blackbody temperature measured in the source frame. Blackbody normalization in units of  $\text{erg cm}^{-2} \text{ s}^{-1}$ . MEKAL (Mewe, Gronenschild, & van den Oord 1985) model normalization in units of and equal to  $\frac{10^{-14}}{4\pi D_A^2 (1+z)^2} \int n_e n_H dV$ , for angular diameter distance  $D_A$ , electron density  $n_e$ , and proton density  $n_H$ .

Table 4: Time-resolved Spectroscopy for GRB 050822

#	Time (s)	BB Flux	$kT$ (keV)	$N_H$	$\chi^2/\nu$	PL Flux	$\Gamma$	$N_H$	$\chi^2/\nu$
WT Mode									
1	111.0-121.0	26.1 ± 1.5	0.66 ± 0.03	0.1 ± 0.1	105.93/59	44.6 ± 3.4	1.8 ± 0.2	1.9 ± 0.6	48.50/59
2	121.0-131.0	28.0 ± 1.6	0.63 ± 0.03	0.1 ± 0.1	107.13/66	51.1 ± 4.0	2.0 ± 0.2	2.7 ± 0.6	53.64/66
3	131.0-141.0	26.1 ± 1.4	0.57 ± 0.03	0.1 ± 0.1	134.80/65	50.0 ± 4.2	2.1 ± 0.2	2.5 ± 0.6	64.32/65
4	141.0-151.0	20.5 ± 1.3	0.54 ± 0.03	0.1 ± 0.1	103.56/54	38.6 ± 3.2	2.0 ± 0.2	1.9 ± 0.6	32.66/54
5	151.0-160.9	16.5 ± 1.2	0.47 ± 0.03	0.1 ± 0.1	85.38/46	33.6 ± 3.9	2.4 ± 0.3	2.4 ± 0.7	33.79/46
6	160.9-170.9	10.1 ± 0.8	0.40 ± 0.04	0.1 ± 0.1	80.37/31	18.2 ± 2.6	2.2 ± 0.4	1.2 ± 0.9	44.87/31
7	170.9-200.9	3.8 ± 0.3	0.35 ± 0.03	0.1 ± 0.1	91.20/36	6.4 ± 0.8	2.3 ± 0.3	0.7 ± 0.7	33.05/36
8	200.9-240.8	3.6 ± 0.3	0.37 ± 0.02	0.1 ± 0.1	80.67/44	7.3 ± 1.2	2.7 ± 0.3	2.2 ± 0.7	39.59/44
9	240.8-280.8	2.7 ± 0.2	0.35 ± 0.03	0.1 ± 0.1	47.69/32	5.5 ± 1.3	3.1 ± 0.4	2.2 ± 0.8	24.38/32
10	280.8-429.6	2.1 ± 0.2	0.34 ± 0.02	0.1 ± 0.1	76.08/52	4.6 ± 1.0	3.1 ± 0.3	2.4 ± 0.7	51.37/52
11	429.6-449.6	10.3 ± 2.3	0.26 ± 0.02	0.7 ± 0.6	33.37/43	81.1 ± 44.3	5.2 ± 0.5	5.6 ± 1.0	30.33/43
12	449.6-469.5	10.0 ± 2.0	0.25 ± 0.02	0.4 ± 0.5	35.46/46	99.6 ± 54.3	5.6 ± 0.5	5.7 ± 1.0	41.03/46
13	469.5-489.5	10.2 ± 4.1	0.20 ± 0.02	0.8 ± 0.8	35.17/37	169.7 ± 72.5	6.7 ± 0.8	6.6 ± 1.4	35.03/37
14	489.5-509.4	6.4 ± 0.7	0.21 ± 0.02	0.1 ± 0.4	51.06/33	53.3 ± 11.1	5.9 ± 0.9	4.8 ± 1.6	54.71/33
15	509.4-549.3	4.1 ± 0.4	0.17 ± 0.02	0.3 ± 0.6	31.63/31	23.6 ± 6.6	6.1 ± 1.0	4.2 ± 1.5	37.11/31
PC Mode									
16	354.4-12823	0.45 ± 0.03	0.27 ± 0.02	0.1 ± 0.1	145.96/38	0.81 ± 0.09	2.1 ± 0.2	0.6 ± 0.2	52.01/38
17	12823-34706	0.19 ± 0.02	0.39 ± 0.05	0.1 ± 0.1	107.85/34	0.40 ± 0.04	2.1 ± 0.3	1.3 ± 0.6	45.42/34
18	34706-88110	0.04 ± 0.01	0.43 ± 0.04	0.1 ± 0.1	72.60/32	0.08 ± 0.01	2.2 ± 0.3	1.6 ± 0.6	31.15/32
PC + WT									
19	549.3-1000.0	1.2 ± 0.3	0.17 ± 0.02	0.3 ± 0.1	48.84/19	12.6 ± 1.3	4.0 ± 1.1	1.2 ± 1.4	35.12/19

Notes: Column density  $N_H$  measured in units of  $10^{21}$  cm $^{-2}$ .  $N_{H,\text{Galactic}} = 2.25 \times 10^{20}$  cm $^{-2}$  (Dickey & Lockman 1990). Power-law (PL) and blackbody (BB) fluxes measured in  $10^{-10}$  erg cm $^{-2}$  s $^{-1}$ , 0.5-10 keV band for PL model. Blackbody temperature measured in the observer frame.

Table 5: Time-resolved Line Search for GRB 050822

#	Time [s]	N lines	Signif.	Line Energy , Equivalent Width , Flux (keV,eV, $10^{-11}$ erg cm $^{-2}$ s $^{-1}$ )
WT Mode				
1	111.0-121.0	0	$< 1.8\sigma$	...
2	121.0-131.0	0	$< 1.7\sigma$	...
3	131.0-141.0	3	$2.1\sigma$	(1.94,93,7.7) (2.91,115,5.9) (3.66,192,7.6)
4	141.0-151.0	0	$< 1.2\sigma$	...
5	151.0-160.9	2	$2.0\sigma$	(1.01,49,5.9) (1.11,51,5.5)
6	160.9-170.9	4	$2.7\sigma$	(0.66,90,7.6) (0.88,67,4.2) (1.13,111,5.5) (1.29,95,4.1)
7	170.9-200.9	0	$< 1.9\sigma$	...
8	200.9-240.8	0	$< 1.5\sigma$	...
9	240.8-280.8	0	$< 0.6\sigma$	...
10	280.8-429.6	0	$< 1.2\sigma$	...
11	429.6-449.6	0	$< 0.6\sigma$	...
12	449.6-469.5	0	$< 1.3\sigma$	...
13	469.5-489.5	0	$< 1.6\sigma$	...
14	489.5-509.4	5	$4.4\sigma$	(0.81,82,3.6) (0.91,142,4.5) (1.04,194,4.3) (1.23,221,3.1) (1.49,265,2.2)
15	509.4-549.3	0	$< 1.9\sigma$	...
PC Mode				
16	354.4-12823	3	$2.5\sigma$	(0.41,75,0.6) (0.63,106,0.5) (3.48,457,0.3)
17	12823-34706	0	$< 1.9\sigma$	...
18	34706-88110	0	$< 2.0\sigma$	...
PC + WT				
19	549.3-1000.0	5	$3.0\sigma$	(0.65,131,1.1) (0.75,64,0.4) (0.82,65,0.3) (0.90,65,0.3) (1.09,50,0.2)

Table 6: Time-resolved Spectroscopy for GRB 050714B

#	Time Reg. (s)	BB Flux	$kT$ (keV)	$N_H$	$\chi^2/\nu$	PL Flux	$\Gamma$	$N_H$	$\chi^2/\nu$
WT Mode									
1	157.4-189.7	$7.1 \pm 1.5$	$0.23 \pm 0.02$	$2.66 \pm 0.59$	33.49/31	$85.49 \pm 40.36$	$5.90 \pm 0.44$	$0.81 \pm 0.09$	29.39/31
PC Mode									
2	221.4-58.3ks	$0.006 \pm 0.001$ $0.033 \pm 0.007$	$0.30 \pm 0.03$ $0.13 \pm 0.03$	$0.30 \pm 0.23$ $3.8 \pm 1.4$	97.19/35 +	$0.015 \pm 0.003$ $0.008 \pm 0.002$	$3.24 \pm 0.28$ $2.2 \pm 0.5$	$0.31 \pm 0.05$ tied	76.78/35 48.64/33
3	275.0-525.0	$0.74 \pm 0.37$ $7.8 \pm 0.4$	$0.22 \pm 0.03$ $0.11 \pm 0.03$	$0.83 \pm 0.69$ $4.5 \pm 2.3$	35.67/19 +	$4.28 \pm 2.69$ $0.7 \pm 0.1$	$5.11 \pm 0.63$ $3.1 \pm 1.1$	$0.53 \pm 0.10$ tied	39.92/19 21.40/17

Notes: Column density  $N_H$  measured in units of  $10^{21}$  cm $^{-2}$ .  $N_{H,\text{Galactic}} = 5.31 \times 10^{20}$  cm $^{-2}$  (Dickey & Lockman 1990). Flux measured in units of  $10^{-10}$  erg cm $^{-2}$  s $^{-1}$ , 0.5-10 keV for the power-law (PL) and bolometric for the blackbody (BB). Blackbody temperature measured in the observer frame.

Table 7: Time-resolved Line Search for GRB 050714B

#	Time [s]	N lines	Signif.	Line Energy , Equivalent Width , Flux (keV,eV, $10^{-12}$ erg cm $^{-2}$ s $^{-1}$ )			
WT Mode							
1	157.4-189.7	0	$<1.8\sigma$	...			
PC Mode							
2	221.4-58.3 ks	4	$4.2\sigma$	(0.91,147,0.09)	(0.76,141,0.12)	(0.56,238,0.35)	(1.12,64,0.03)
3	275.0-525.0	4	$3.4\sigma$	(0.74,170,57.5)	(0.59,340,261)	(0.93,108,16.0)	(0.83,68,15.4)

Table 8: Spectroscopy of Bright ( $> 10$  cts/s peak) XRT Flares

Burst	Time Reg. (s)	Fluence ( $10^{-7}$ erg cm $^{-2}$ )	$\Gamma$	$N_H$ ( $10^{21}$ cm $^{-2}$ )	$\chi^2/\nu$
050502b	400-1200	$6.61 \pm 0.09$	$2.43 \pm 0.03$	$1.76 \pm 0.07$	373.28/357
050607	250-600	$0.38 \pm 0.03$	$2.29 \pm 0.13$	$2.11 \pm 0.36$	30.78/34
050712	150-300	$0.55 \pm 0.02$	$2.06 \pm 0.10$	$2.35 \pm 0.32$	91.62/73
050713A	95-150	$3.07 \pm 0.10$	$2.31 \pm 0.06$	$5.55 \pm 0.25$	216.45/207
050714B	275-525	$1.07 \pm 0.67$	$5.11 \pm 0.63$	$5.25 \pm 1.02$	39.92/19
050730	130-300	$1.43 \pm 0.04$	$1.63 \pm 0.05$	$1.69 \pm 0.21$	178.00/171
050730	300-600	$1.90 \pm 0.04$	$1.72 \pm 0.05$	$1.02 \pm 0.14$	215.10/227
050730	600-800	$0.84 \pm 0.03$	$1.84 \pm 0.07$	$0.43 \pm 0.18$	127.01/134
050820	215-252	$2.40 \pm 0.06$	$0.99 \pm 0.05$	$1.87 \pm 0.23$	202.11/207
050822	410-650	$4.03 \pm 0.50$	$4.95 \pm 0.13$	$4.07 \pm 0.24$	141.36/127
050904	350-600	$1.37 \pm 0.03$	$1.73 \pm 0.05$	$1.49 \pm 0.15$	221.51/227
051117A	1250-1725	$6.81 \pm 0.09$	$2.31 \pm 0.03$	$1.94 \pm 0.08$	368.05/364
051117A	800-1250	$4.77 \pm 0.08$	$2.32 \pm 0.03$	$1.76 \pm 0.09$	333.41/307
060111A	200-500	$5.59 \pm 0.09$	$2.29 \pm 0.03$	$2.70 \pm 0.10$	355.60/335
060124	300-650	$16.48 \pm 0.13$	$1.39 \pm 0.02$	$2.36 \pm 0.07$	611.60/611
060124	650-900	$12.91 \pm 0.13$	$1.92 \pm 0.02$	$2.26 \pm 0.08$	486.54/453
060204B	100-270	$1.95 \pm 0.05$	$2.00 \pm 0.05$	$2.78 \pm 0.19$	168.65/201
060204B	270-450	$0.25 \pm 0.02$	$2.68 \pm 0.13$	$2.88 \pm 0.34$	78.40/70
060210	100-165	$1.32 \pm 0.03$	$1.82 \pm 0.06$	$2.04 \pm 0.20$	149.31/157
060210	165-300	$2.70 \pm 0.05$	$1.92 \pm 0.04$	$1.98 \pm 0.14$	210.08/260
060210	350-450	$1.18 \pm 0.07$	$2.93 \pm 0.08$	$2.86 \pm 0.21$	127.92/141
060312	100-200	$0.14 \pm 0.01$	$2.30 \pm 0.09$	$2.99 \pm 0.29$	72.11/105

Table 9: Line Detections in the Bright ( $> 10$  cts/s peak) XRT Flares

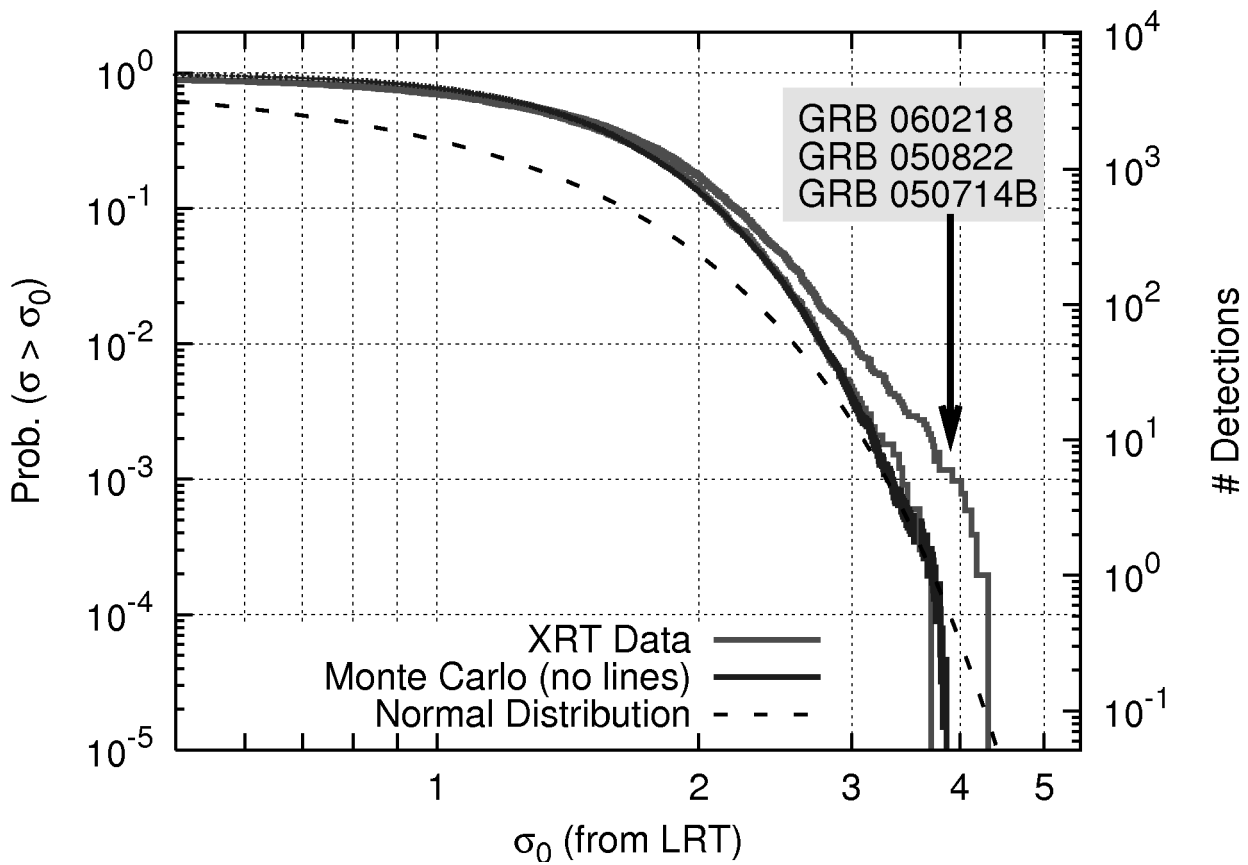
Burst	Time [s]	N lines	Signif.	Line Energy , Equivalent Width , Flux (keV,eV, $10^{-11}$ erg cm $^{-2}$ s $^{-1}$ )
050502b	400-1200	4	$3.6\sigma$	(1.44,15,0.4) (1.69,18,0.4) (4.48,57,0.3) (2.14,17,0.2)
050607	250-600	5	$2.1\sigma$	(2.11,152,0.2) (0.79,62,0.4) (0.61,118,1.1) (3.29,409,0.3) (2.57,216,0.3)
050712	150-300	0	$<1.9\sigma$	...
050713A	95-150	3	$2.9\sigma$	(1.82,40,4.1) (4.48,97,3.0) (3.72,65,2.6)
050714B	275-525	3	$3.4\sigma$	(0.74,162,6.9) (0.59,301,30.7) (0.93,98,1.7)
050730	130-300	1	$2.2\sigma$	(1.97,53,0.7)
050730	300-600	5	$2.9\sigma$	(1.12,31,0.4) (1.41,29,0.3) (1.01,27,0.4) (1.87,47,0.5) (0.77,18,0.3)
050730	600-800	0	$<1.9\sigma$	...
050820	215-252	2	$2.3\sigma$	(4.27,72,4.9) (1.96,41,2.8)
050822	410-650	3	$3.9\sigma$	(0.91,22,2.8) (0.61,44,30.9) (2.06,76,0.3)
050904	350-600	0	$<1.7\sigma$	...
051117A	1250-1725	3	$4.4\sigma$	(1.88,34,0.9) (2.83,26,0.4) (0.60,25,3.0)
051117A	800-1250	4	$4.3\sigma$	(1.75,30,0.6) (1.37,20,0.5) (0.92,16,0.7) (1.05,12,0.4)
060111A	200-500	4	$2.3\sigma$	(1.80,20,0.7) (1.04,12,0.9) (0.90,11,0.9) (0.80,10,1.0)
060124	300-650	3	$3.2\sigma$	(1.89,18,1.2) (4.57,29,1.4) (3.47,18,0.9)
060124	650-900	5	$2.6\sigma$	(3.20,28,1.5) (4.51,40,1.6) (4.89,42,1.6) (1.12,8,1.2) (2.73,18,1.1)
060204B	100-270	4	$2.8\sigma$	(2.64,61,1.7) (2.08,44,1.5) (2.83,56,1.4) (4.32,83,1.4)
060204B	270-450	0	$<1.8\sigma$	...
060210	100-165	0	$<1.6\sigma$	...
060210	165-300	0	$<1.3\sigma$	...
060210	350-450	1	$2.1\sigma$	(0.62,50,8.7)
060312	100-200	1	$2.5\sigma$	(0.60,117,1.7)

Table 10: Afterglow Energetics Parameters

Burst	$z$	$E_{\gamma,iso}$ [ $10^{51}$ erg]	$L_{X,t=10hrs}$ [ $10^{44}$ erg s $^{-1}$ ]	$S_{BB}$ [ $10^{51}$ erg]	$\delta t_{BB}$ [s] [s]
060218	0.033	$0.062 \pm 0.003$	$0.013 \pm 0.003$	$0.23 \pm 0.07$	$\sim 300$
060202	0.783	$4.4 \pm 0.4$	$43 \pm 11$	$1.3 \pm 0.4$	$\lesssim 1000$
050822	1.2	$15 \pm 1$	$410 \pm 80$	$0.43 \pm 0.18$	$\sim 100$
050714B	2.66	$13 \pm 2$	$440 \pm 90$	$2.8 \pm 1.0$	$\sim 200$

Notes: Redshifts  $z$  for GRBs 060202, 050822, and 050714B are inferred from the X-ray spectroscopy (Section 4).

Cumulative Line Detections (500 cts spectra)





Cumulative Line Detections (500 cts spectra)

